



# Numerical modeling of dispersion of swimming bacteria in a Poiseuille flow

A. Ganesh, C. Douarche, M. Dentz, Harold Auradou

## ► To cite this version:

A. Ganesh, C. Douarche, M. Dentz, Harold Auradou. Numerical modeling of dispersion of swimming bacteria in a Poiseuille flow. *Physical Review Fluids*, 2023, 8 (3), pp.034501. 10.1103/PhysRevFluids.8.034501 . hal-03903970v2

**HAL Id: hal-03903970**

**<https://hal.science/hal-03903970v2>**

Submitted on 6 Mar 2023

**HAL** is a multi-disciplinary open access archive for the deposit and dissemination of scientific research documents, whether they are published or not. The documents may come from teaching and research institutions in France or abroad, or from public or private research centers.

L'archive ouverte pluridisciplinaire **HAL**, est destinée au dépôt et à la diffusion de documents scientifiques de niveau recherche, publiés ou non, émanant des établissements d'enseignement et de recherche français ou étrangers, des laboratoires publics ou privés.

# Numerical modeling of dispersion of swimming bacteria in a Poiseuille flow

A. Ganesh , C. Douarche

*Université Paris-Saclay, CNRS, FAST, 91405, Orsay, France*

M. Dentz\*

*Spanish National Research Council (IDAEA-CSIC), Barcelona, Spain*

H. Auradou

*Université Paris-Saclay, CNRS, FAST, 91405, Orsay, France*

(Dated: March 6, 2023)

## Abstract

This paper reports a numerical study of the dispersion of bacteria modelled as active Brownian ellipsoids placed in a plane Poiseuille flow. The longitudinal (along the flow direction) and transverse (along the direction perpendicular to the plane of flow) macroscopic dispersion coefficients are determined from the analysis of a large number of trajectories and their scaling are studied as function of the Péclet number  $Pe$ . Three different regimes are observed: (i) at low shear rate, rotational diffusion associated to the swimming activity of the bacteria dominates and classical Taylor dispersion regime is observed. In this regime, the longitudinal dispersion coefficient scales like Péclet square. (ii) an intermediate "active" regime, where the shear induces a reorientation of the bacteria. This increases the longitudinal dispersion that scales as  $Pe^{2+\kappa}$ , with  $\kappa$  ranging between 1.5 and 2 for aspect ratio between 10 and 1. In this regime, the dispersion coefficient in the direction perpendicular to the plane of the flow decreases like  $\log(1/Pe)$ . (iii) a final "new" Taylor regime, where the diffusivity in the gap is set by the molecular diffusion coefficient. We also show that the "active" regime originates from the enhancement in the time taken by particles to diffuse across the channel gap. We further show that, decreasing the channel height delayed the transition to the "active" regime.

---

\* marco.dentz@csic.es

## I. INTRODUCTION

Dispersion of bacteria by a flow in confined environment influences many processes such as the spreading and contamination of soils by harmful microorganisms or their ability to find and colonise new niches in natural environments. One of the key questions is the characterisation of the bias introduced by a flow on their swimming trajectories and its influence on the macroscopic hydrodynamic transport. By allowing to track bacteria under various flow conditions, microfluidics has proven to be a remarkable tool to learn more about the coupling between bacteria and flow [1]. Since bacteria have a tendency to accumulate on surfaces, many studies have largely focused on the motion of swimming bacteria on surfaces [2–7]. A wide range of behaviours like upstream motions [3, 5], transverse motion [6], or oscillations on the surface induced by the rheotactic torque on the flagella [8] are observed by these studies. Away from the surfaces, bacteria are observed to perform helicoidal trajectories [9–11] similar to the trajectories obtained analytically by Jeffery [12] for an elongated particle immersed in a sheared viscous fluid. In confined geometry, the bacteria also have the possibility to explore the flow profile across the channel gap and are thus exposed to a gradient of shear rates while swimming. This is particularly true in microfluidic devices, and this results in the migration of the bacteria towards high shear regions [11]. This phenomenon, known as high shear trapping increases the presence of the bacteria close to surfaces, where shear is the highest [11, 13, 14]. The reverse has also been predicted numerically *i.e.* the trapping of bacteria in low shear regions [15]. The trapping of the bacteria in flow regions will have significant effect on their macroscopic transport. One of the key focuses of the present work is to study the effect of trapping on the macroscopic scale *viz* the influence of the competition between convection by the flow along Jeffery orbits and mixing between the flow lines on macroscopic longitudinal dispersion. To understand the physics at play, we considered a situation where bacteria are transported in a Poiseuille flow, such as characterising flow in fractured media.

In a fluid at rest, flagellated bacteria such as *Escherichia coli* alternate between two phases of motion [16] : run (motion in essentially straight paths performed at a constant swimming velocity  $V_s$ ) and tumble (random change in orientation). This behaviour leads to a 3D diffusive motion with a diffusion coefficient  $D_0$ . The same diffusive behaviour is obtained with particles that gradually change their swimming direction by rotational diffusion with an angular diffusivity  $D_R$  [17]. Such particles diffuse with a diffusion coefficient  $D_0 = \frac{V_s^2}{6D_R} + D_m$ , where  $D_m$  is the molecular diffusion

coefficient. This  $D_m$  would be the diffusion coefficient measured if the bacteria were to lose their swimming ability. Based on this analogy, Langevin models that incorporate the convection, the reorientation and the rotation by the flow can be derived [11, 18, 19]. In those approaches, the bacteria are usually modelled as self-propelling elongated ellipsoid of aspect ratio  $q$  that move and rotate according to the following equations [18]:

$$\dot{\mathbf{x}} = V_s \mathbf{p} + \mathbf{u} + \sqrt{\frac{2D_m}{\tau}} \boldsymbol{\xi}_x \quad (1)$$

$$\dot{\mathbf{p}} = [\mathbf{I} - \mathbf{p}\mathbf{p}].\left[\left(\frac{q^2 - 1}{q^2 + 1}\right)\mathbf{E} - \mathbf{W}\right].\mathbf{p} - 2D_R \mathbf{p} - \sqrt{\frac{2D_R}{\tau}} \mathbf{p} \wedge \boldsymbol{\xi}_p \quad (2)$$

where  $\mathbf{x}$  and  $\mathbf{p}$  are the particle position and orientation. In the above equations, the particle is convected by the local flow velocity  $\mathbf{u}$  characterized by its local strain rate tensor  $\mathbf{E} = [\nabla \mathbf{u} + \nabla \mathbf{u}^T]/2$  and its local vorticity tensor  $\mathbf{W} = [\nabla \mathbf{u} - \nabla \mathbf{u}^T]/2$ . The Gaussian white noise  $\boldsymbol{\xi}$  has zero mean and unit variance. In this work, Eq.(2) is interpreted in the Ito sense. It should be kept in mind that the model neglects the finite size of the particles and therefore neglects the hydrodynamic perturbation of the swimming activity on the fluid and is inaccurate very close to the walls, where steric interaction occurs. As shown in Raible and Engel [20], this formulation describes motion on the unit sphere, which implies that the norm of  $\mathbf{p}$  is conserved and equal to 1. In Eq.(1), molecular diffusion coefficient  $D_m$  is included, such contribution is often assumed negligible [11, 18] but was found to have an important effect on the asymptotic regime [13] and is considered in our study. In the absence of coupling between the particle re-orientation and the flow (referred as decoupled case), the particle gets convected at the local flow velocity. Its influence is balanced by diffusion across the gap. This results in a macroscopic Fickian dispersion parallel to the flow characterized by the equation [21, 22]:

$$\frac{D_{\parallel}}{D_0} = 1 + \frac{4}{210} Pe^2 \quad (3)$$

where Péclet number  $Pe = \frac{UH}{D_0}$  represents the ratio between the diffusion time in the gap  $\tau_{taylor} = H^2/2D_0$  and the convective time  $2H/U$ . The objective of this work is to study how Eq.(3) is modified when the effect of shear and vorticity on the orientation of the particles is taken into account.

Analytical solution of the set of equations (1) exists for Couette flow (*i.e.* constant shear rate  $\dot{\gamma}$ )

and for  $D_m = 0$  [11]. Those studies revealed that the probability distribution of the orientation of the particles depends on a single dimensionless number that compares the time scale of the flow  $\dot{\gamma}$  and the time scale for bacteria to reorient due to their swimming activity  $D_R$ . For small flow Péclet number  $Pe_f = \frac{\dot{\gamma}}{D_R}$  all orientations are equally probable but an emergence of a preferential orientation, increasingly aligned with the flow direction, is observed with increase in  $Pe_f$  [23, 24]. For Poiseuille flows, a second dimensionless number the swimming Péclet number  $Pe_s$  equivalent to the Knudsen number for gas that compares the reorientation time scale of the swimmer  $1/D_R$  and the time  $2H/V_s$  for the bacteria to swim across the gap of size  $2H$  was introduced [13]. For wide channels such as  $Pe_s = V_s/2HD_R \ll 1$ , bacteria are found to migrate either to the surfaces [11, 13] or towards the center of the channel [15] depending on the aspect ratio of the particles and the flow Péclet number. At larger values of  $V_s/2HD_R$  the rheotactic effects of the surface becomes predominant and greatly affects the dispersion of particles [13, 25]. The question we address in the present study concerns the consequence of the coupling between particle orientation and flow on the emergence of these low and high shear trapping mechanisms as well as on the macroscopic longitudinal (direction of flow) and transverse (perpendicular to the plane of flow) dispersion. We also study its effect on the relaxation time scale (time scale needed to reach the asymptotic regime across the channel gap).

We performed 3D Langevin simulations on the equations of motion (cf. Eqs.(1) and (2)) to obtain the macroscopic dispersion coefficients in presence of coupling between the particle orientation and flow. The details of the simulations is presented in Sec. II. In section III, the macroscopic longitudinal dispersion coefficient obtained,  $D_{||}$ , is studied as function of the Péclet number and bacteria aspect ratio. This section allows to identify an "active" dispersion regime characterized by a dispersion coefficient increasing as a power law of the Péclet number with an exponent larger than 2. We will show that this new exponent mainly reflects the dependence of the relaxation time scale with the shear rate. We will also demonstrate the distribution profile of the bacteria in the gap in this "active" dispersion regime. Sec. III.2, we will further show that the increase of the dispersion in the flow direction is associated with a reduction of the dispersion in the direction perpendicular to the plane of the flow. In Sec. III.3 and III.4, the effect of the molecular diffusion of the bacteria and the aperture on the domain of existence of the "active" dispersion will be addressed. Finally, conclusions and some perspectives are provided in sections IV and V respectively.

## II. MATERIALS AND METHODS

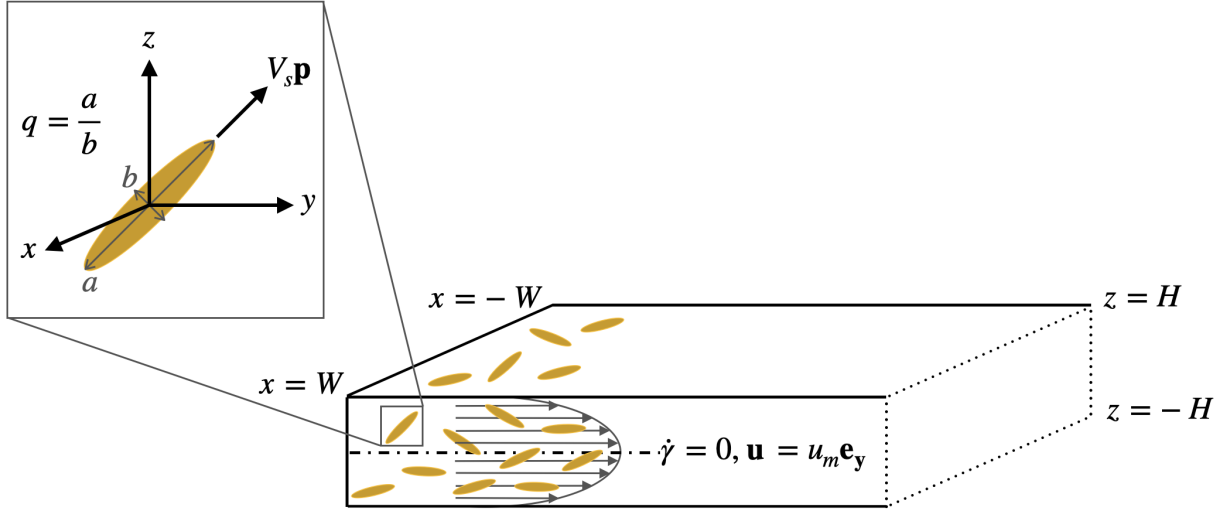


FIG. 1: Schematic representation of a population of swimming bacteria placed in Poiseuille flow.  $x$  is the transverse direction,  $y$  is the direction of flow and  $z$  is the direction of height (vertical). Individual bacteria modelled as active Brownian ellipsoid swimming with an orientation  $\mathbf{p}$ . The aspect ratio of the particles is  $q = \frac{a}{b}$  where  $a$  is the particle length and  $b$  the particle width.

The swimming bacteria were modelled as elongated ellipsoids of aspect ratio  $q$  located in a Cartesian system of reference coordinates by their positions  $\mathbf{x}_i(t)$  ( $x, y, z$ ) and orientation  $\mathbf{p}_i(t)$  ( $p_x, p_y, p_z$ ) where  $i$  is associated to particle index. The particles were subjected to a Poiseuille flow (See fig.1) whose velocity profile is given by:

$$u(z) = \frac{3U}{2} \left[ 1 - \left( \frac{z}{H} \right)^2 \right] \quad (4)$$

where  $U$  is the average flow velocity. The local shear rate is :  $\dot{\gamma}(z) = \frac{du(z)}{dz} = -\frac{3Uz}{H^2}$  and is maximal on the surface *i.e.* for  $z = \pm H$  with  $\dot{\gamma}_m = \frac{3U}{H}$ . This characteristic value of the shear rate is used in the definition of the flow Péclet number.

All particles in the system were assumed to be identical. They have the same aspect ratio  $q$ , the same swimming velocity  $V_s$ , the same rotational diffusion coefficient  $D_R$  and the same molecular diffusion coefficients  $D_m$ . For  $q > 1$ , the long axis of the particle and its swimming direction are aligned. The case of  $q = 1$  corresponds to a spherical swimmer. Finally,  $q < 1$  corresponds to a

particle which swims along the direction of its minor axis. A value of  $q \gg 1$  is typical of natural microswimmers like bacteria. For instance, recent studies found that *E. coli* bacteria trajectories can be well adjusted by an active rod of an aspect ratio  $q \simeq 10$  [11, 18]. Any other value of  $q$  could be characteristic of an artificial microswimmer.

Their positions and orientations were tracked by integrating Eq.(1) and (2) with a time step  $\tau$  and by drawing at each time step and for each particle random numbers from a Gaussian distribution of zero mean and unit variance. The discrete version of these equations is given in appendix B. The choice of the integration time step  $\tau$  is detailed in Appendix C. The equations of motions were simultaneously solved for  $10^5$  trajectories. The particles were initially uniformly distributed in  $x$  and  $z$  directions and were situated at  $y = 0$ . The particles were confined in the  $x$  and  $z$  directions between parallel surfaces located at  $x = -W$  and  $x = W$  and at  $z = -H$  and  $z = H$  respectively.  $W$  was fixed at 3 cm and  $H$  was varied such that  $W/H \gg 1$  always.

Surfaces are considered steric boundaries [26, 27], that is, when a particle arrives at a boundary it moves along the surface until it undergoes a reorientation away from the surface and swims back into the bulk. These conditions named SBC for Steric Boundary Conditions) allow to reproduce the large residence times and the persistence of bacteria swimming along the surfaces as observed experimentally [7, 28]. Some simulations were done with reflective boundary conditions (referred to RBC) to examine the effect of swimming persistence along surfaces on the results and allow comparison with published studies [14].

At each time step, the first moment  $m_{1k}(t)$  and the variance  $\sigma_k^2(t)$  of the distribution of the population of particles were estimated in all three direction  $k : x, y, z$  as:

$$m_{1k}(t) = \langle k(t) - k(0) \rangle, \quad (5)$$

$$\sigma_k^2(t) = \langle (k(t) - k(0) - m_{1k}(t))^2 \rangle \quad (6)$$

where  $\langle \cdot \rangle$  is the average over all particles.

The Fig. 2 (a) shows the variation of the rate of change  $\sigma_y^2(t)$  as function of  $t$  for three flow conditions. The following trend was observed for all the cases: a first linear regime followed by a plateau. With this representation, the plateau regime corresponds to the diffusive regime. The relaxation time  $\tau_c$  to transit to the diffusive regime was observed to be affected by the flow con-

ditions used. Increasing the flow Péclet number clearly delays the transition to diffusive regime. Practically, the two values  $D_{\parallel}$  and  $\tau_c$  were obtained by adjusting the data by the function :

$$\frac{d\sigma_y^2(t)}{dt} = 2D_{\parallel}(1 - e^{-t/\tau_c}) \quad (7)$$

In Fig. 2 (b) the variation of the variance in the gap  $\sigma_z^2(t)$  scaled with  $H^2$  is shown as function of time for the same flow conditions as in Fig. 2(a). The variance initially increases with time indicating that the particle explores the gap which corresponds to the linear regime observed on Fig. 2(a). At  $t > \tau_c$ ,  $\sigma_z^2(t)$  plateaus to a constant value indicating that the particles have explored the entirety of the gap. This corresponds to the asymptotic diffusive regime described before.

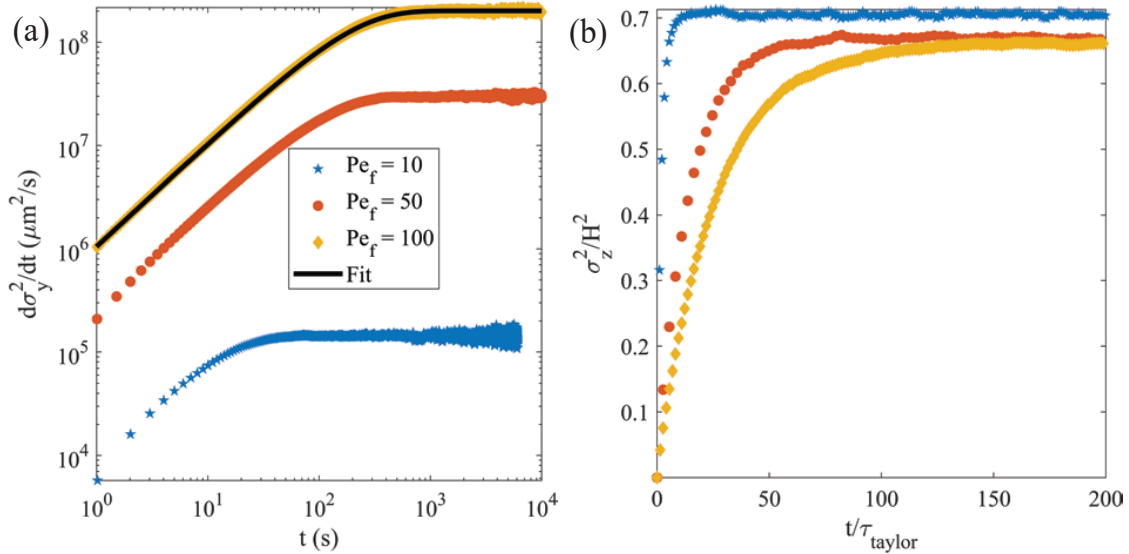


FIG. 2: (a) Rate of change of the second moment in the flow direction  $\frac{d\sigma_y^2(t)}{dt}$  plotted as function of time for different flow Péclet  $Pe_f$ . The black line corresponds to a fit performed using Eq. 7. (b) Scaled second moment in  $z$ -direction plotted as function of time scaled with Taylor time scale for different  $Pe_f$ .  $\star$ ,  $\bullet$  and  $\blacklozenge$  are respectively for  $Pe_f = 10, 50$  and  $100$  which corresponds to Péclet numbers of respectively  $Pe = 125, 625$  and  $1250$ . Dashed line fit with Eq. (7) of the  $Pe_f = 100$  case. For all three cases:  $q = 2$ ,  $2H = 100\mu\text{m}$ ,  $D_m = 1\mu\text{m}^2\text{s}^{-1}$ .

In the following sections, the variations of  $D_{\parallel}$  and  $\tau_c$  are studied as function of the flow and bacteria characteristics. They are often compared with the diffusion coefficient measured in absence of flow,  $D_0$ , and the corresponding Taylor's diffusive time scale  $\tau_{taylor} = H^2/2D_0$ . Practically, simulations without coupling with the flow vorticity and shear were achieved by setting  $\mathbf{E}$  and  $\mathbf{W}$  to zero. These cases are referred to as decoupled cases. Unless explicitly mentioned, all the



simulations were done by setting  $D_R = 1 \text{ rad}^2/\text{s}$  and  $V_s = 20 \text{ } \mu\text{m}/\text{s}$  values typically observed for motile bacteria [29]. The Péclet numbers range from 1 to 2500.

### III. RESULTS

#### III.1. Effect of the particle aspect ratio on the longitudinal dispersion coefficient

In this section, we present results that focuses on the effect of shear coupling on the longitudinal dispersion  $D_{\parallel}$  and relaxation time scale  $\tau_c$ . The molecular diffusion coefficient is neglected ( $D_m = 0$ ) for these cases. For this condition, the Péclet number and the flow Péclet number are related by the relation:  $Pe = 2 \frac{D_R^2 H^2}{V_s^2} Pe_f$ . We also set the distance between the two plates to  $2H = 100 \mu\text{m}$ . Therefore, we have  $Pe = 12.5 Pe_f$ .

The longitudinal dispersion coefficient  $D_{\parallel}$  obtained for different flow conditions and particle aspect ratios are represented in Fig.3. For the decoupled case (Filled circles in Fig.3), the results of the simulation fall onto the theoretical prediction made by Taylor [21, 22, 30], that predicts an increase of the longitudinal dispersion coefficient like the square of the Péclet. In the other cases, the simulations first gave  $D_{\parallel}$  values very close to the values predicted by Taylor. However, for  $Pe > 100$  (*viz*  $Pe_f > 10$ ), a deviation from Taylor model is observed. The difference increases with the Péclet number and  $D_{\parallel}$  increases faster than  $Pe^2$ . We recover here the "giant active Taylor–Aris dispersion" regime reported by Dehkharghani *et.al* [19].

To understand the origin of the deviation, we determined separately the two terms that contribute to the dispersion: the velocity variance of the particles  $\sigma_{U_p}^2$  and the relaxation time scale  $\tau_c$ . These two terms are related to the dispersion coefficient by the relation  $D_{\parallel} \sim \sigma_{U_p}^2 \tau_c$  [31]. Practically, the variance  $\sigma_{U_p}^2$  of the particle velocity is calculated from the components of the particle velocities along the flow direction at the end of the simulation. In this way, we have  $t \gg \tau_c$  and the profiles have reached their asymptotic form. In the situation considered by Taylor, the particles diffuse freely across the streamlines without any effect of the local fluid shear or fluid vorticity and the particles are uniformly distributed in the gap. In this case, the relaxation time is constant with  $\tau_c \sim \tau_{taylor}$ , the time to diffuse across the gap, and is independent of Péclet number. In the limit of a negligible effect of diffusion (*i.e.*  $Pe \gg 1$ ), the variance of the particle and fluid velocities are identical. For a Poiseuille flow, we have:  $\sigma_{U_p}^2 = \sigma_U^2 = \frac{1}{5} U^2$ .

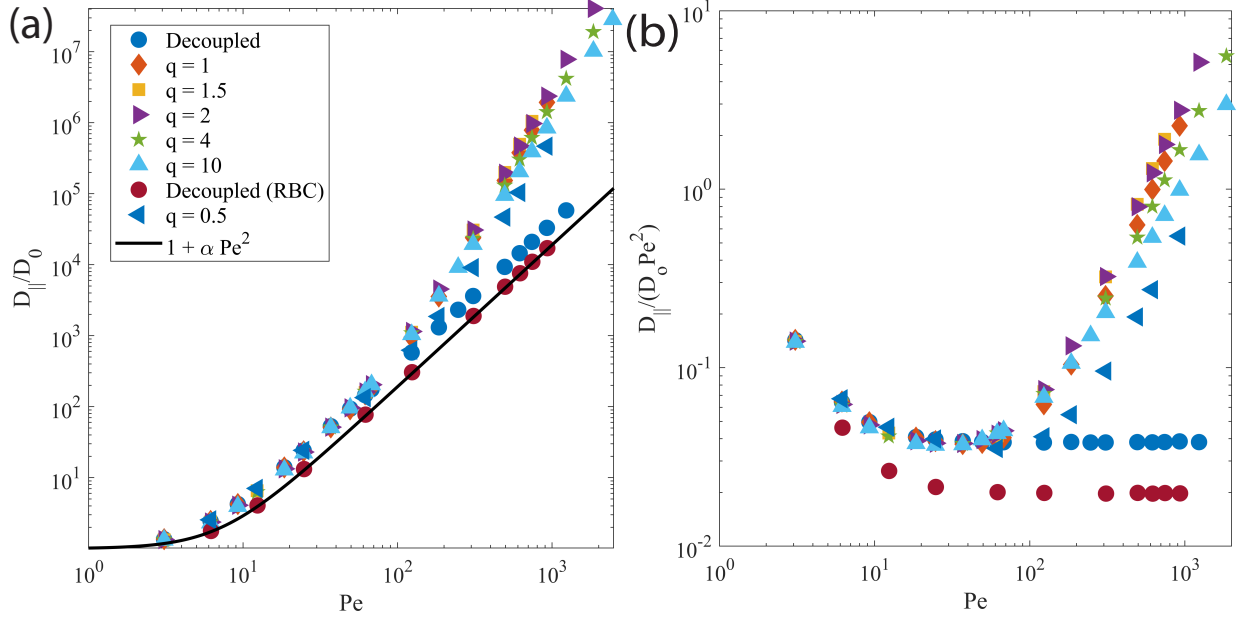


FIG. 3: (a) Longitudinal dispersion coefficient  $D_{||}$  normalized by the diffusion coefficient measured in absence of flow  $D_0$  as function of the Péclet number  $Pe = \frac{UH}{D_0}$ . The solid line is the Taylor prediction  $1 + \frac{4}{210}Pe^2$  [21, 22]. (b)  $D_{||}/D_0$  scaled with respect to  $Pe^2$ . • are for decoupled cases (blue: SBC and maroon: RBC)

. ◀, ◆, ■, ▶, ★ and ▲ are respectively for particles of aspect ratios  $q = 0.5, 1, 1.5, 2, 4$  and  $10$  respectively. Data obtained for  $2H = 100\mu\text{m}$  and  $D_m = 0$ .

Figs. 4(a) and (b) shows that these predictions are well obtained in the decoupled case with reflecting boundaries conditions (RBC): (i)  $\sigma_{U_p}^2/U^2$  plateaus to a value close to  $1/5$  for  $Pe > 100$  (See Fig.4(a)) and (ii)  $\tau_c/\tau_{taylor}$  is constant at all Péclet number (See Fig.4(b)). If the bacteria have the option of swimming along the surfaces (Blue circles in Fig.4), they will spend more time in regions of zero fluid velocity. This condition increases the normalized variance of the velocities, as can be seen in Fig.4(a). The blue circles plateau to a value close to  $0.3$ . As for the relaxation time (See Fig.4(b)), it remains constant and independent of the Péclet number, as for the case of RBC, but with a slightly higher value. The consequence is an increase of the dispersion coefficient, which however still varies as Péclet squared as shown in Fig. 3.

We will now look at how these two terms are modified when the particles are coupled with shear. The Fig.4(a) shows the variation of  $\sigma_{U_p}^2$  normalized by  $U^2$  to be first decreasing with in-

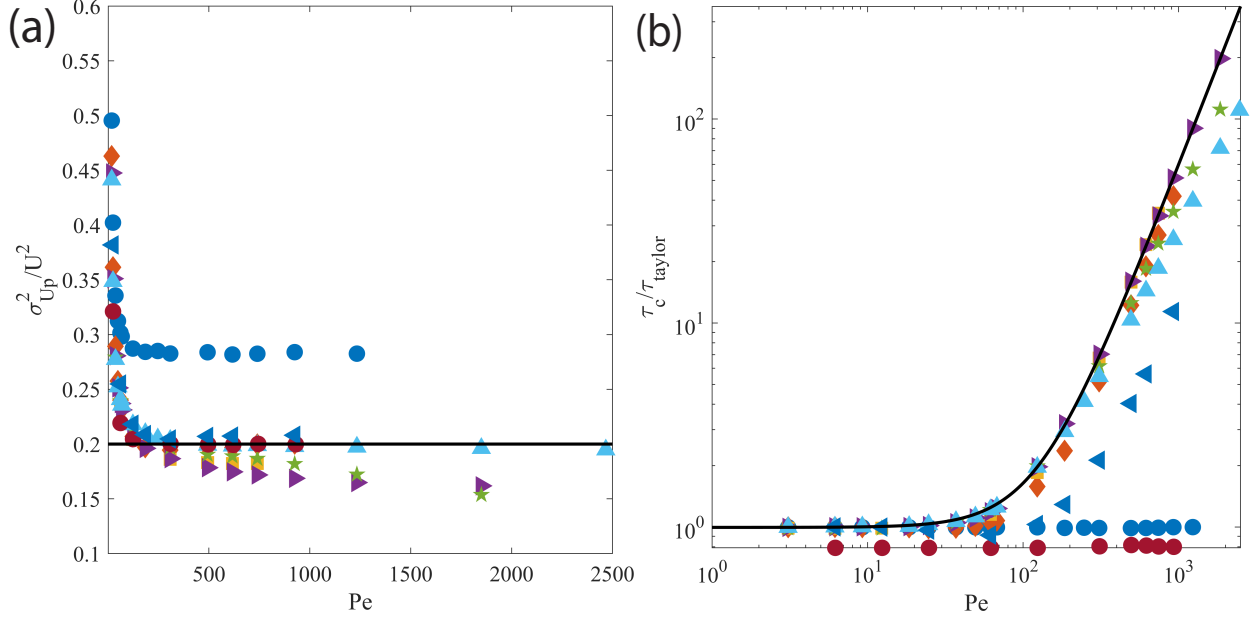


FIG. 4: (a) Evolution of the normalized variance of the particle velocity  $\sigma_{U_p}^2/U^2$  as function of the Péclet number  $Pe = \frac{UH}{D_0}$ . (b) Log-Log representation of the normalized relaxation time  $\tau_c/\tau_{taylor}$  as function of  $Pe$ .  $\blacktriangleleft, \blacklozenge, \blacksquare, \blacktriangleright, \star$  and  $\blacktriangle$  are for particles of aspect ratios  $q = 0.5, 1, 1.5, 2, 4$  and  $10$  respectively.  $\bullet$  shows the decoupled case (in (a) reflective BC case has also been included). Solid line: fit by  $1 + \beta Pe^\kappa$  of the  $q = 2$  case. The data were obtained with  $2H = 100\mu\text{m}$ ,  $D_m = 0$ .

crease in  $Pe$ . This regime is where the transport of particles is dominated by diffusion. This is followed by a transition regime between  $Pe \sim 50 - 100$  and then by a new regime for  $Pe > 100$  (viz  $Pe_f > 10$ ) where the transport of the particles is dominated by the imposed shear. In this regime, the values of  $\sigma_{U_p}^2$  normalized by  $U^2$  converge to values between 0.16 and 0.2. Now, let us take a look at Fig 4(b), which shows the variation of the normalized relaxation time  $\tau_c/\tau_{taylor}$  as function of  $Pe$ . For  $Pe < 100$  (viz  $Pe_f < 10$ ), we observe the relaxation time is constant. In this limit, the reorientation by the diffusion due to swimming activity dominates and particles diffuse in the gap as they do in absence of flow, and we have  $\tau_c \sim \tau_{taylor}$ . As the flow increases, shear increasingly aligns the particles along the flow direction. This in turn reduces the diffusivity of the particles across the gap which results in the increase in relaxation time as shown in Fig 4 (b). In this new regime, we observe that  $\tau_c$  varies as a power law of the Péclet number with an exponent  $\kappa$ . Thus,  $D_{||}$  increases as  $Pe^{2+\kappa}$  for these cases.

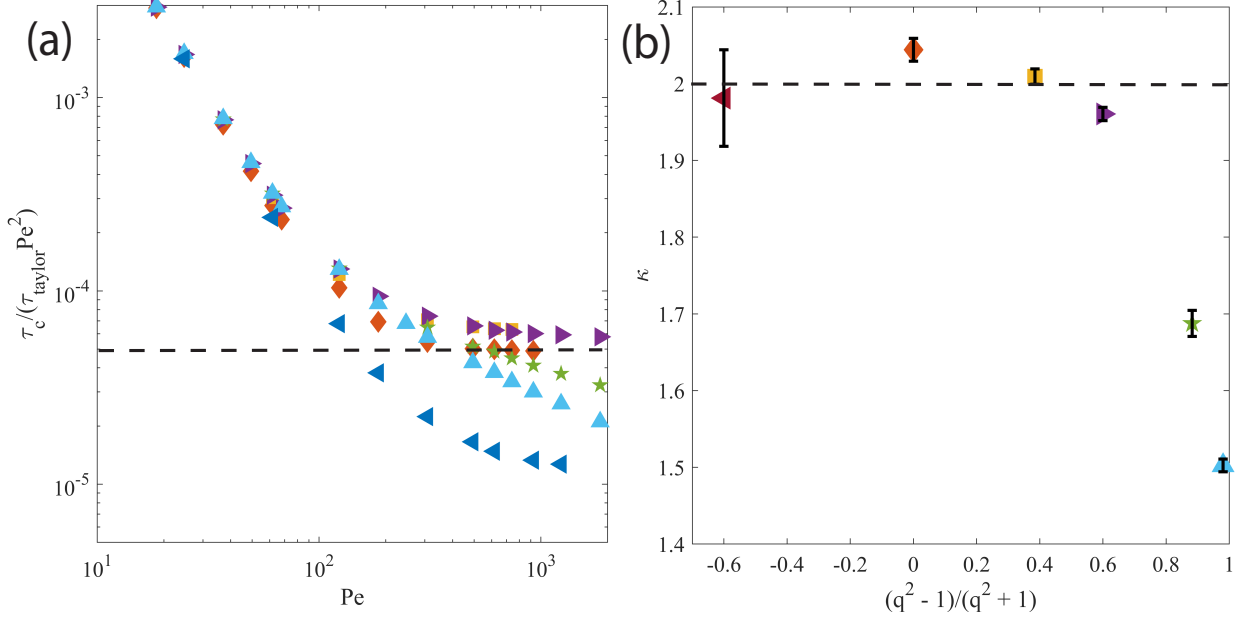


FIG. 5: (a) Log-Log representation of  $\tau_c/\tau_{\text{taylor}}$  scaled with  $Pe^2$  as function of  $Pe$  for different  $q$ . The horizontal dashed line is a guide to mark the asymptotic regime reached by small  $q$ . (b)  $\kappa$  as function of Bretherton constant  $\frac{q^2 - 1}{q^2 + 1}$ .  $\blacktriangleleft$ ,  $\blacklozenge$ ,  $\blacksquare$ ,  $\blacktriangleright$ ,  $\star$  and  $\blacktriangle$  are for particles of aspect ratios  $q = 0.5, 1, 1.5, 2, 4$  and  $10$  respectively. The horizontal dashed line shows the value of  $\kappa$  obtained from the model proposed in appendix E. The data were obtained with  $2H = 100\mu\text{m}$ ,  $D_m = 0$ .

Dehkharghani *et al.* [19] report a  $Pe^4$  variation of  $D_{\parallel}$  and this would indicate  $\kappa = 2$ . To check this, we first plotted  $\tau_c/\tau_{\text{taylor}}$  normalized by  $Pe^2$  as shown in Fig. 5(a). We observe that the value initially decreases for small  $Pe$ , which corresponds to the diffusion dominated regime where  $\tau_c/\tau_{\text{taylor}}$  is constant. At high  $Pe$  and for  $q < 4$ , we observe that  $\tau_c/\tau_{\text{taylor}}$  normalized by  $Pe^2$  to reach an asymptotic horizontal plateau (see the  $\blacklozenge$ ,  $\blacksquare$ ,  $\blacktriangleright$  and  $\blacktriangleleft$  symbols in Fig. 5(a)). This indicates that,  $\kappa \simeq 2$  for these aspect ratios. However, for the case of  $q = 4$  and  $10$ , we observe that they are still decreasing with  $Pe$  (see  $\star$  and  $\blacktriangle$  symbols in Fig. 5(b)), implying that  $\kappa < 2$ . The  $\kappa$  estimated by fitting  $\tau_c/\tau_{\text{taylor}}$  vs  $Pe$  data points with  $1 + \beta Pe^{\kappa}$  are shown in Fig. 5 (b). We observe the  $\kappa$  values to be very close to 2 for  $q = 0.5, 1, 1.5$  and  $2$ . This is followed by a decrease in  $\kappa$  and they are  $\sim 1.7$  and  $1.5$  respectively for  $q = 4$  and  $q = 10$ . This double variation i.e. change in variance of velocities as  $U^2$  (which is the case of Taylor dispersion) with a pre-factor as function of the aspect ratio, as well as change in relaxation time as  $Pe^{\kappa}$ , where  $\kappa \sim f(q)$  results in a overall deviation of the macroscopic longitudinal dispersion  $D_{\parallel}$  from Taylor with  $D_{\parallel} \sim Pe^{2+\kappa}$ . The fact that this effect is observed only in the case where the effect of local shear on the particle

reorientation is taken into account, underlines the importance of shear alignment on the increase of the macroscopic longitudinal dispersion of bacteria.

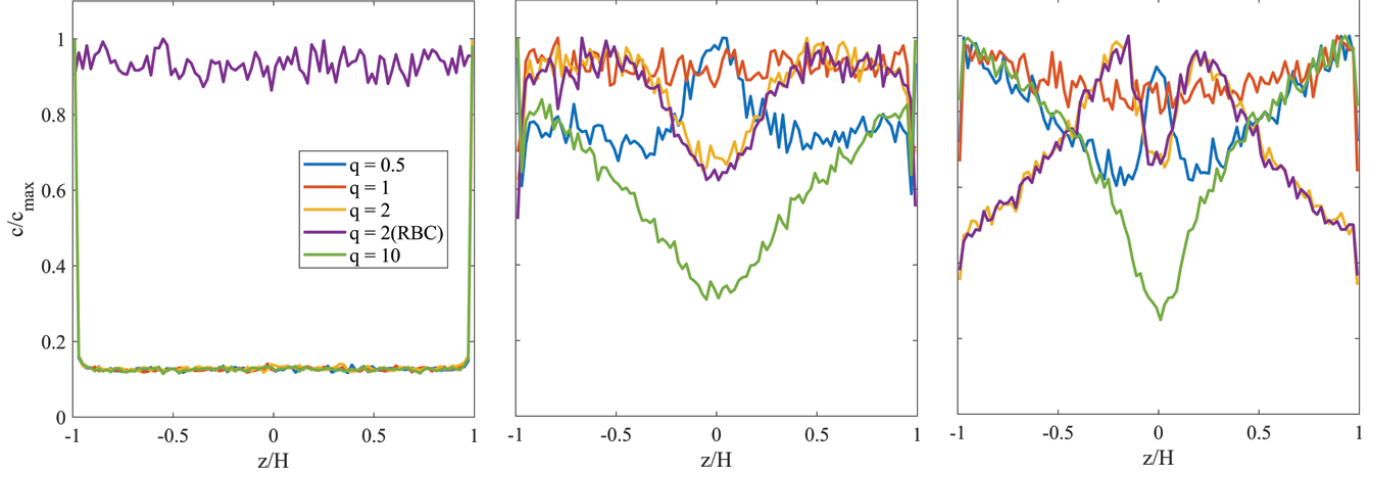


FIG. 6: Particle distributions in the gap for (a): ( $Pe_f = 0.5$ ,  $Pe = 6.25$ ), (b): ( $Pe_f = 25$ ,  $Pe = 312.5$ ) and (c): ( $Pe_f = 75$ ,  $Pe = 937.5$ ) and for four aspect ratios :  $q = 0.5, 1, 2$  and  $10$ . Profiles obtained with RBC at  $q = 2$  (purple curves) are also shown. The data were obtained with  $2H = 100\mu\text{m}$  and  $D_m = 0$ .

To identify the consequence of shear-coupling on the localisation of particles in the gap, we plot the particle distribution for different aspect ratios and Péclet numbers as shown in Fig. 6. First, we will focus on the profiles far from the surfaces, i.e. at normalized distances  $z/H$  between  $-0.9$  and  $0.9$ , and consider the evolution of the profiles with the Péclet number and with the aspect ratio of the particles. At low Péclet, the particles are uniformly distributed in the gap. This regime corresponds to the regime where the longitudinal dispersion of the particles coincides with Taylor dispersion ( $D_{||}/D_0 \sim Pe^2$ ). When  $Pe$  increases above  $100$  (which corresponds to  $Pe_f > 10$ ), we observe a shift in the distribution of the particles across the gap. For instance, at an intermediate  $Pe = 312.5$  (Fig. 6 (b)), we observe both  $q = 2$  (yellow curve) and  $10$  (green curve) to exhibit high shear trapping (bacteria accumulate in regions close to the surfaces). However,  $q = 10$  particles exhibit a stronger depletion at the centre compared to  $q = 2$  particles. As we increase the  $Pe$  to about  $937.5$ , particles with  $q = 2$  exhibit low shear trapping (particles tend to accumulate in the center of the channel) whereas bacteria with  $q = 10$  (green curve) still exhibit high shear trapping. High shear trapping can be differentiated from low shear trapping based on the slope of the particle distribution close to the channel surfaces [14]. The change of the sign of the slope from negative

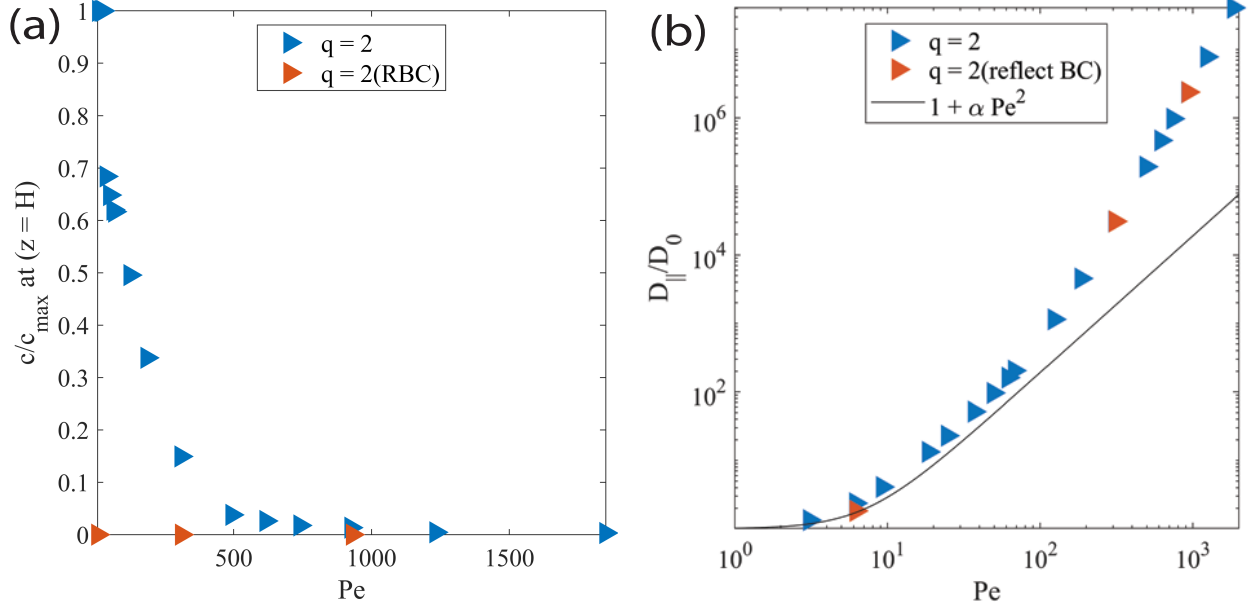


FIG. 7: (a) Normalized number of particles on the surface as function of the Péclet number (b) Longitudinal dispersion coefficient  $D_{||}$  normalized by the diffusion coefficient measured in absence of flow  $D_0$  as function of the Péclet number. The solid line is the Taylor prediction  $1 + \frac{4}{210}Pe^2$  [21, 22]. The data were obtained with  $q = 2$ ,  $2H = 100\mu\text{m}$  and  $D_m = 0$ . Blue triangles: SBC and red triangles: RBC.

to positive when going from high shear trapping to low shear trapping allows us to establish a phase diagram giving the type of trapping observed as a function of the flow Péclet number and the aspect ratio of the particles. The phase diagram obtained by applying this criterion is shown in Fig. 8. It can be compared to the diagram obtained by Vennamneni et al. [14] by solving the 1D Fokker-Planck equation. At low  $Pe_f$ , the concentration profile is constant in the aperture and the dispersion regime is the same as the Taylor dispersion observed for passive tracers and for which  $\kappa = 0$ . This regime is replaced by a high shear trapping regime when the flow Péclet number becomes greater than 10. The value of the flow Péclet number which characterizes the transition between uniform distribution ( $\bullet$ ) to high shear trapping ( $\blacklozenge$ ) is not observed to depend on the aspect ratio of the particles. However, with increase in  $Pe_f$ , we observe that the high shear trapping regime ( $\blacklozenge$ ) evolves into a low shear trapping regime ( $\blacksquare$ ). The threshold separating these two regimes increases with the aspect ratio of the particles. It occurs for  $Pe_f$  between 40 and 50 for aspect ratios of 1.5 or 2 and moves to larger values of  $Pe_f$  as  $q$  increases. The values for which the transition is observed are of the order of those obtained by Vennamneni et al. [14]. For

$q=10$ , we note a difference between our simulations and those of Vennamneni *et al.* [14]. Our model predicts a transition between the two trapping modes for a flow Péclet number of 300, while Vennamneni *et al.* [14] observes a transition for a flow Péclet number between 120 and 200. This delay of the transition to larger flow Péclet numbers might come from the confinement: the study of Vennamneni *et al.* [14] considered wide channels for which the swimming Péclet is small i.e.  $Pe_s \ll 1$  whereas our model allows to change this parameter and to explore its influence on dispersion. In the case of Fig. 8, we have  $Pe_s = 0.2$ . The influence of confinement will be addressed in Sec. III.4.

Vennamneni *et al.* [14] also showed that the particle depletion observed in the centre of the flow in the low shear trapping regime, evolves and finally collapses for particles with large  $q$ . This depletion in the particle distribution is visible in 17(c)-(e) in appendix D. However, in the range of  $Pe_f$  explored in this study, we do not observe a complete collapse of swimmer concentration at the centreline. Accumulation in the centre of the flow is however, here, observed for particles with aspect ratios of 0.5 (blue curves in Fig. 6) when  $Pe_f > 10$ . This regime then results in the co-existence of both low and high shear trapping. This indicates that, these type of particles, exhibits "jumps" from the highest to lowest shear region and spend little time in the other flow streamlines across the channel gap. The case of spherical particles ( $q = 1$ ) shows no trapping and the particles are uniformly distributed across the channel gap. This observation is in agreement with the Langevin simulation performed by Rusconi *et al.* [11].

The distribution of particles near the surfaces also evolves with the flow Péclet number. At very low flow Péclet numbers, the SBC boundary conditions give rise to a very strong accumulation on the surface (See Fig. 6(a)). This accumulation not observed when RBC are used (Purple curve in Fig. 6(a)). In this case, the same number of particles is observed on the surfaces vicinity and in the fluid. When the flow Péclet number is increased, two effects are seen: (i) the number of bacteria on the surface drops, and (ii) this is accompanied by a depletion zone of small extension that finally joins the distribution profile in the fluid. The first effect is illustrated in Fig. 7(a) where we plot the number of bacteria whose  $z$ -positions are  $-H$  or  $H$ . We see a continuous drop of the number of bacteria. These two effects leads, at the highest flow Péclet number (See Fig. 6(c)), to a situation where the maximum of the particle distribution is no longer at the surface. The depletion zone in the surface vicinity is observed for both boundaries conditions (RBC and SBC). As we will see in

Sec. III.4, its dimension decreases with the flow Péclet number and is independent of the channel aperture. Its presence is thus particularly identifiable on simulations done with small  $H$ . This is why this depletion layer is not found in Vennamneni *et al.* [14] study which is restricted to wide channels.

Finally, we observe that at high  $Pe$ , the two boundaries conditions used have a weak influence on the steady state distribution (see collapse of yellow and purple curves in Figs. 6 (b) and (c)) and thus on the macrodispersion (see Fig. 7(b)).

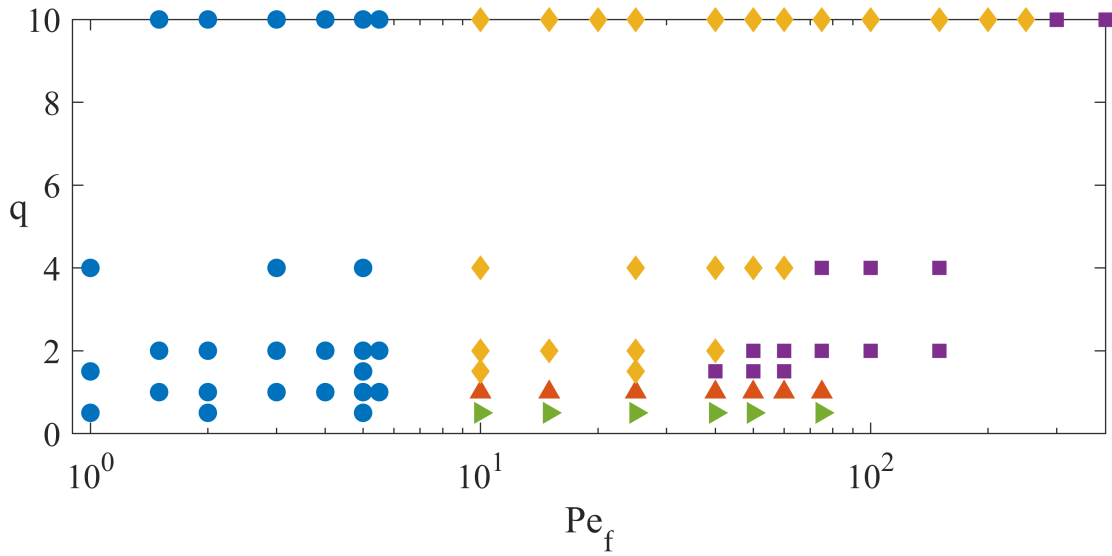


FIG. 8: Phase diagram depicting the different regimes in the steady state concentration profiles across the channel gap observed for different  $q$  as function of the flow Péclet number  $Pe_f = \frac{\gamma_m}{D_R}$ . (i)  $\bullet$ : Uniform distribution of particles across the channel gap with accumulation on the surface, (ii)  $\blacktriangle$ : Uniform distribution across channel gap with slight depletion on the surface, (iii)  $\blacklozenge$ : High shear trapping, (iv)  $\blacksquare$ : Low shear trapping and (v)  $\blacktriangleright$ : co-existence of high and low shear trapping. Data obtained for  $2H = 100\mu\text{m}$  and  $D_m = 0$  with SBC and for  $Pe_s = 0.2$ . It is to be noted that  $Pe$  defined by Vennamneni *et al.* [15] corresponds to  $Pe_f/2$ .

### III.2. Effect of the aspect ratio on the dispersion coefficient transverse to the plane of the flow

To determine the dispersion coefficient in the direction transverse to the plane of the flow, the variation of the variance of the transverse position of the bacteria  $\sigma_x^2$  as function of time was



studied. The dispersion coefficient  $D_x$  was then obtained by fitting the rate of change of  $\sigma_x^2$  using the same method as for obtaining  $D_{\parallel}$ . Fig. 9 shows  $D_x$  as function of Péclet number for swimmers with different aspect ratios.

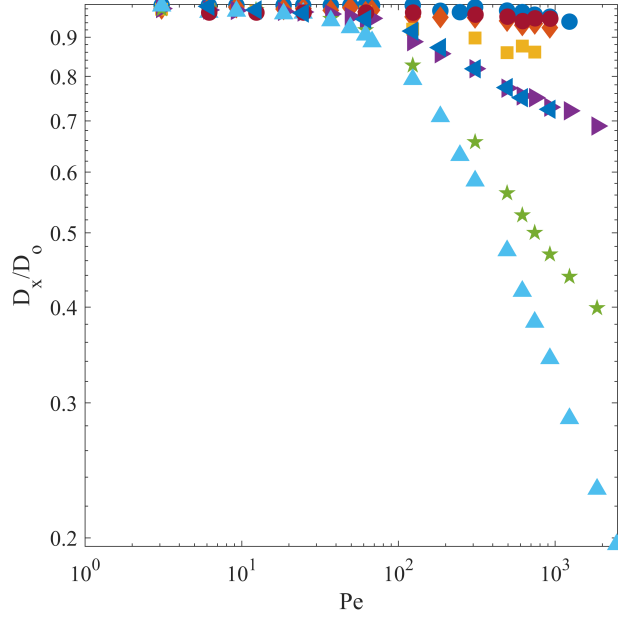


FIG. 9: Normalized dispersion coefficient measured in the direction transverse to the plane of flow as function of the Péclet number.  $\bullet$  are for the decoupled case.  $\blacktriangleleft$ ,  $\blacklozenge$ ,  $\blacksquare$ ,  $\blacktriangleright$ ,  $\star$  and  $\blacktriangle$  are for particles of aspect ratios  $q = 0.5, 1, 1.5, 2, 4$  and  $10$  respectively.  $2H = 100\mu\text{m}$ ,  $D_m = 0$ .

In the decoupled case (circles in Fig. 9), the dispersion coefficient remains very close to the dispersion coefficient  $D_0$  as what we observe in the flow direction. When the coupling with the flow is taken into account, we find the three regimes observed previously: (i) the flow is first not strong enough to have a significant influence on the dispersion of the bacteria ( $Pe < 10$ ), (ii) we then have a transition zone for Péclet between 10 and 100 and (iii) a domain in which the coupling controls the dispersion. The latter domain is reached for a flow Péclet greater than 10. In contrast to the longitudinal direction, we observe a reduction of the transverse dispersion coefficient. This reduction is slow with  $D_x$  which varies as  $\log(1/Pe)$ . We also observe that the reduction is more important for bacteria with a large aspect ratio. This is due to the fact that, as we increase the shear, the particle displaces longer in the longitudinal direction before reorientation. Even though there is no flow imposed in  $x$  – *direction*, there will be repercussions due to imposed flow on the diffusivity because of the shear-coupling effect as well as the interdependence of the orientation

of particles in one direction with other two directions i.e.  $p_x = f(\dot{\gamma}(z), p_y, p_z)$  (c.f. Eq.(B4) in Appendix B).

### III.3. Effect of molecular diffusion on the longitudinal dispersion coefficient

In the previous sections, the effect of molecular diffusion was neglected. In this section, we study its influence on the relaxation time  $\tau_c$  and longitudinal dispersion  $D_{\parallel}$  of the bacteria. In absence of flow, the diffusion coefficient is now given by:  $D_0 = \frac{V_s^2}{6D_R} + D_m$ . In addition to  $\tau_{taylor}$ , we can define a second time scale with respect to  $D_m$ :  $H^2/2D_m$ . We make use of the latter to define a new Péclet number:  $Pe_c = \frac{UH}{D_m}$ . To get as close as possible to the conditions of bacteria which have a characteristic size of the order of a micron meter, simulations were carried out with a molecular diffusion coefficient ranging from  $0.05$  to  $20 \mu\text{m}^2 \text{s}^{-1}$  which corresponds to characteristic sizes of bacteria between  $0.01$  and  $4 \mu\text{m}$ .

In figures 10 and 11, the influence of  $D_m$  for a fixed aspect ratio  $q = 2$  and a channel gap of  $2H = 100 \mu\text{m}$  are presented. It can be seen from Fig. 11 that there is a decrease in relaxation time with increase in  $D_m$ . A direct correlation is seen with the longitudinal dispersion coefficient of the particles as well in Fig 10(a). Three distinct regimes are observed. At low  $Pe$ , the longitudinal dispersion exhibits a Taylor behaviour where the diffusion is dominated by the effective diffusivity of the particles  $D_0$ . Then, there is an intermediate "active" regime where the longitudinal dispersion deviates from the Taylor regime. Finally, as depicted in Fig. 10(b), the longitudinal dispersion collapses back into a new "passive" Taylor regime where the diffusive time scale is defined by  $D_m$  and the diffusion is controlled purely by the molecular diffusion coefficient. The transition from the "active" intermediate regime to the final "passive" Taylor regime is a function of  $D_m$  i.e. higher the  $D_m$  the sooner the transition occurs. If the  $D_m$  is chosen to be of same order or of higher order than  $\frac{V_s^2}{6D_R}$  the effect of activity would fully be suppressed by  $D_m$ . This result corroborates one of the results by Vennamneni *et. al.* [14] where it was concluded by the author that the critical  $Pe$  at which the transition from "active" regime to "passive" Taylor regime is inversely proportional to the magnitude of  $D_m$ . As shown by Vennamneni *et al.* [14], we also observe that the presence of  $D_m$  shifts the steady state distribution of particles in the gap towards a uniform distribution from high/low shear trapping at high shear rates. We also observe that this effect is in direct correspondence to the limit of  $\tau_{taylor}/\tau_c$  reaching a new asymptotic value corresponding to the final value

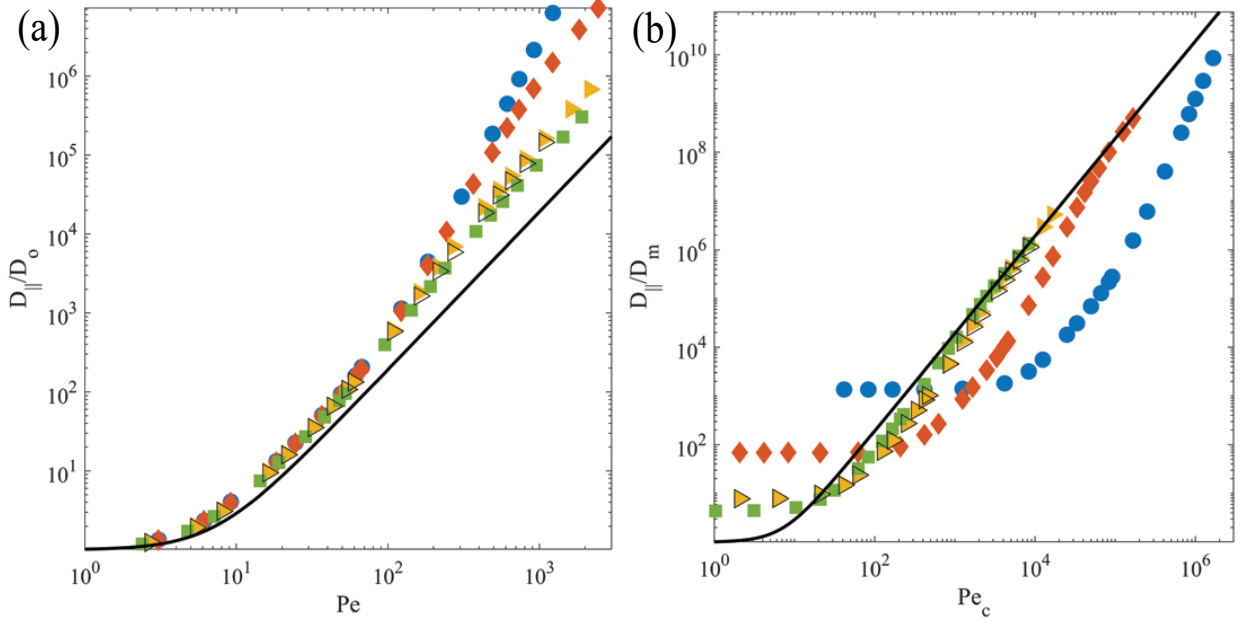


FIG. 10: (a) Longitudinal dispersion coefficient normalized by the diffusion coefficient  $D_0$  measured in absence of flow as function of the Péclet number  $Pe = \frac{UH}{D_0}$ . The solid line is the Taylor prediction  $\frac{D_{\parallel}}{D_0} = 1 + \frac{4}{210}Pe^2$  [21, 22]. (b) Longitudinal dispersion coefficient normalized by  $D_m$  as function of the Péclet number  $Pe_c = \frac{UH}{D_m}$ . The solid line is the Taylor prediction  $\frac{D_{\parallel}}{D_m} = 1 + \frac{4}{210}Pe_c^2$ . For all plots: ( $\bullet$ :  $D_m = 0.05 \mu\text{m}^2 \text{s}^{-1}$ ,  $q = 2$ ), ( $\blacklozenge$ :  $D_m = 1 \mu\text{m}^2 \text{s}^{-1}$ ,  $q = 2$ ), ( $\blacktriangleright$ :  $D_m = 10 \mu\text{m}^2 \text{s}^{-1}$ ,  $q = 2$ ), ( $\blacktriangleright$ :  $D_m = 10 \mu\text{m}^2 \text{s}^{-1}$ ,  $q = 10$ ), and ( $\blacksquare$ :  $D_m = 20 \mu\text{m}^2 \text{s}^{-1}$ ,  $q = 2$ ).

at which the longitudinal dispersion converges to the "passive" Taylor regime where the diffusion across the gap becomes independent of the imposed shear rate.

Now, let us focus on the effect of  $D_m$  on the dispersion of bacteria of different aspect ratio. We fix  $D_m = 10 \mu\text{m}^2 \text{s}^{-1}$  and we consider  $q = 2$  and  $q = 10$ . We observe in Figures 10 and 11, that the behaviors for the two aspect ratios are very similar. Thus, molecular diffusion suppresses the effect of the aspect ratio on the dispersion of particles. This shows that the effect of molecular diffusion is significant not only in the macroscopic dispersion of particles of a given aspect ratio, but also mitigates the effect of shape on the longitudinal dispersion and relaxation time scales.

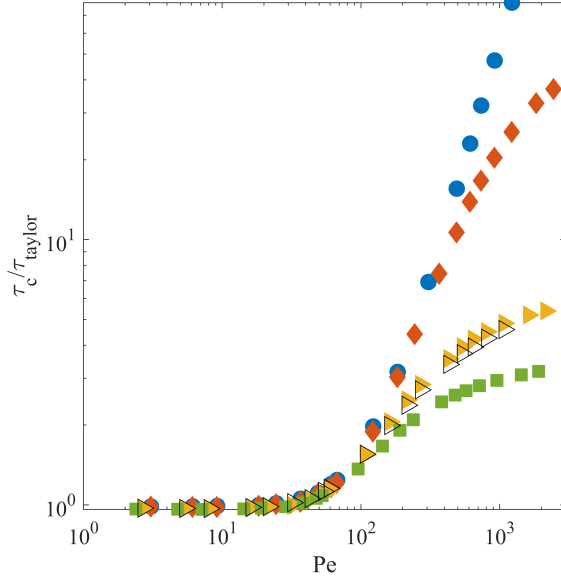


FIG. 11: Evolution of the normalized relaxation time  $\tau_{taylor}/\tau_c$  as function of the Péclet number  $Pe$  for ( $\bullet$ :  $D_m = 0.05 \mu\text{m}^2 \text{s}^{-1}$ ,  $q = 2$ ), ( $\blacklozenge$ :  $D_m = 1 \mu\text{m}^2 \text{s}^{-1}$ ,  $q = 2$ ), ( $\blacktriangleright$ :  $D_m = 10 \mu\text{m}^2 \text{s}^{-1}$ ,  $q = 2$ ), ( $\blacktriangleleft$ :  $D_m = 10 \mu\text{m}^2 \text{s}^{-1}$ ,  $q = 10$ ), and ( $\blacksquare$ :  $D_m = 20 \mu\text{m}^2 \text{s}^{-1}$ ,  $q = 2$ ).

#### III.4. Influence of gap height on the longitudinal dispersion

This section focuses on the influence of channel gap height  $2H$  on the dispersion of the particles of a given aspect ratio  $q = 2$  and in absence of molecular diffusion ( $D_m = 0$ ). The simulations were performed for 4 different swimming Péclet numbers ranging between 0.04 and 0.67. The different values of  $Pe_s$  were obtained by changing the channel aperture from 30 to 500  $\mu\text{m}$  without changing the swimming characteristics of the bacteria. The Fig. 12 shows the change in longitudinal dispersion with respect to  $Pe_f$ . We observe that for  $Pe_f > 10$ , the curves deviate from Taylor's prediction to reach the asymptotic power law regime described in Sec. III.1. The power law fit of the data at large  $Pe_f$  gives the same value for all three apertures with  $\kappa \simeq 1.96$ . We also see that  $D_{||}$  is larger for  $2H = 500 \mu\text{m}$  at a given  $Pe_f$  than for  $2H = 30 \mu\text{m}$ . This is because for a given  $Pe_f$ , the  $U$  is larger for  $2H = 500 \mu\text{m}$  case than for  $2H = 30 \mu\text{m}$ .

From Fig. 13(a) where the normalized variance of particle velocity is plotted as function of  $Pe_f$ , we observe that the normalized variance collapses to the asymptotic value in the same manner as in Fig 4(b). This indicates that the velocity variance scales as  $Pe_f^2$ . We also observe that the

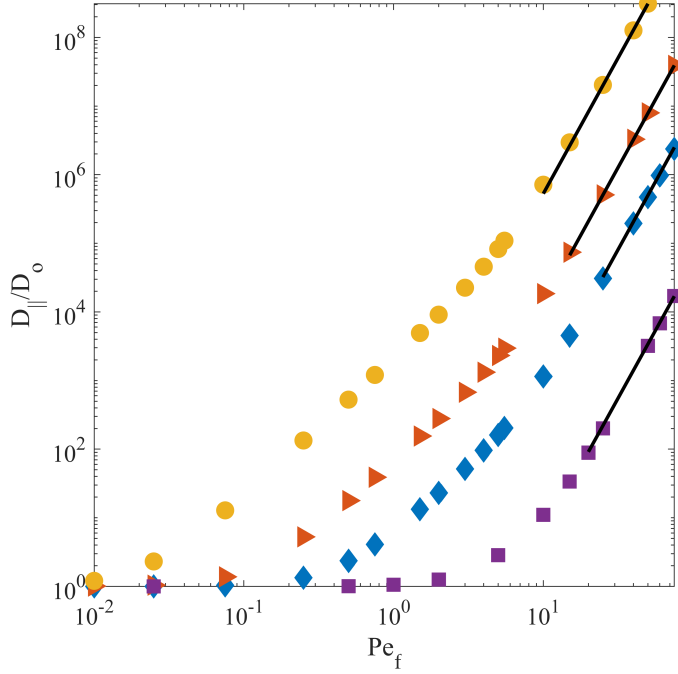


FIG. 12: Longitudinal dispersion coefficient normalized by the diffusion coefficient  $D_0$  measured in absence of flow as function of the flow Péclet number  $Pe_f = \frac{\dot{\gamma}_m}{D_R}$ . ■, ♦, ► and • are respectively for  $2H = 30, 100, 200$  and  $500 \mu\text{m}$ . Data obtained for:  $q = 2$  and  $D_m = 0$ . Solid lines of slope  $2 + \kappa$  with  $\kappa = 1.96$  are also plotted to highlight the power law variation  $D_{||} \propto Pe_f^{2+\kappa}$ .

Data obtained for:  $q = 2$  and  $D_m = 0$ .

transition from the diffusive regime (at low  $Pe_f$ ) to the "active" regime (at high  $Pe_f$ ) occurs at a lower  $Pe_f$  for the wider channels (cf. Fig. 13 (a) and (b)). Decreasing the aperture, therefore, delays the onset of the "active" regime. For  $Pe_f < 10$ , we also observe in Fig. 13(b) that the plateau values of  $\tau_c/\tau_{\text{taylor}}$  decrease when  $2H$  is increased. This is due to a decrease in the surface accumulation with increase in channel height as shown in Fig. 14. This can be explained as follows. The swimming Péclet number,  $Pe_s = \frac{V_s}{2HD_R}$  decreases with increase in  $2H$ . Therefore the frequency at which a particle encounters the surface is reduced leading to a decrease in the surface effect. At large  $2H$  and small  $Pe_f \ll 1$ ,  $\tau_c/\tau_{\text{taylor}}$  plateaus to a value close to the one observed in Fig. 4(b) for decoupled simulations performed with RBC.

Let us now return to the depletion zone appearing near the surfaces. As we have seen in Sec. III, this depletion is present for both boundary conditions used (RBC or SBC). To confirm this a simulation was performed in a channel with a small height under both boundary conditions. The

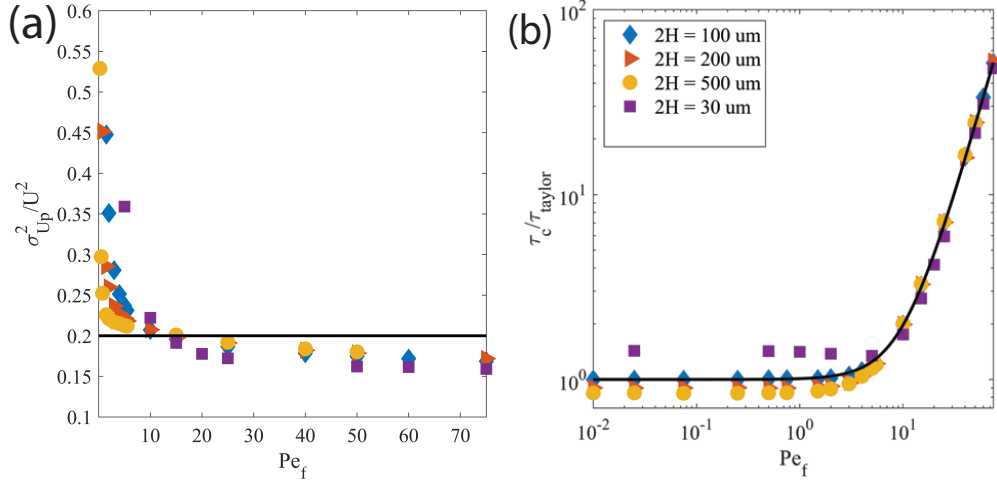


FIG. 13: (a) Normalized variance of particle velocity as function of flow Péclet number  $Pe_f = \frac{\dot{\gamma}_m}{D_R}$ . Horizontal solid line: value of  $\sigma_{Up}^2/U^2$  for a parabolic profile. (b) Evolution of the normalized relaxation time  $\tau_{taylor}/\tau_c$  as function of the flow Péclet number  $Pe_f = \frac{\dot{\gamma}_m}{D_R}$ .  $\blacksquare$ ,  $\blacklozenge$ ,  $\blacktriangleright$  and  $\bullet$  are respectively for  $2H = 30, 100, 200$  and  $500 \mu m$ . Data obtained for:  $q = 2$  and  $D_m = 0$ .

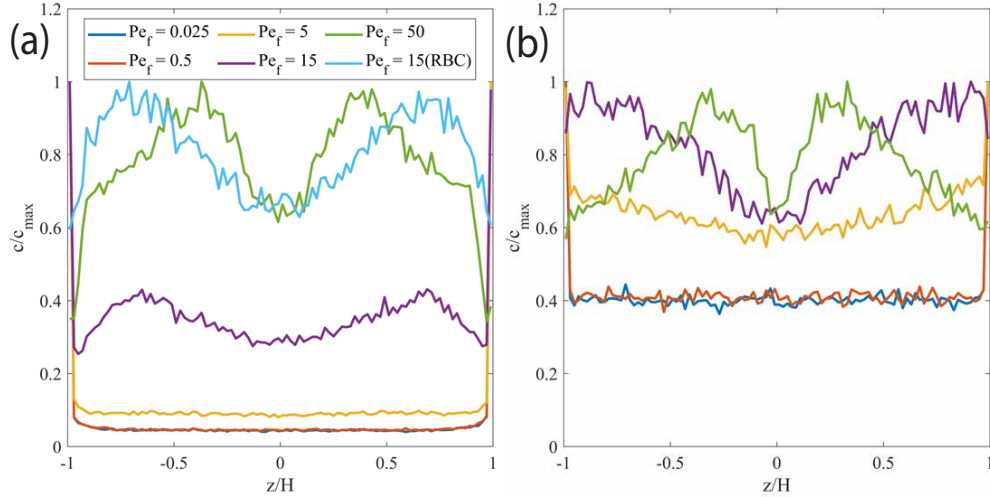


FIG. 14: Concentration profiles in the channel gap for different flow Péclet number  $Pe_f = \frac{\dot{\gamma}_m}{D_R}$ . (a)  $2H = 30 \mu m$  (b)  $2H = 500 \mu m$  Data obtained for:  $q = 2$  and  $D_m = 0$ .

concentration profiles obtained for the same flow Péclet are represented in Fig. 14(a) by the blue and purple curves. Because of the accumulation on the surface, the purple curve is lower than the blue curve. Apart from this difference already discussed in Sec. III, we observe the same decrease near the surfaces, i.e. for a normalized distance  $z/H$  between -1 and -0.75 or between 0.75 and 1. This depletion zone narrows when the flow Péclet increases. This results in a depletion zone for

the green curve (obtained for  $Pe_f = 50$ ) being closer to the surfaces than the purple curve (obtained with  $Pe_f = 15$ ). The size of the depletion layer extends over about 5 microns for  $Pe_f = 15$  and it will become difficult to detect its presence when the height  $H$  increases. For instance, its presence is hardly discernible on the profiles shown in Fig. 14(a) obtained for  $2H = 500\mu\text{m}$ . We believe that this zone results from the combined effect of the near-surface vorticity and the reflective conditions which influence the probability density function of the particle. The extension of this zone is proportional to the persistence length  $V_s/Dr$  of the swimmer and its size decreases with the flow Péclet number. This is because, the projection of the swimming velocity along the  $z$  direction decreases with the shear rate.

#### IV. DISCUSSION AND CONCLUSIONS

Our study demonstrates that shear alignment of bacteria by flow increases the longitudinal dispersion coefficient. The consequence of shear alignment on dispersion is observed when the flow Péclet number  $Pe_f$  is larger than 10. Below this critical value, diffusion due to the swimming activity is strong enough to reduce the effect of shear alignment. Bacteria diffuse in the gap like passive Brownian particles with a diffusive time scale given by the diffusion coefficient  $D_0$  associated to the random swimming motion of the particle.

For  $Pe_f > 10$ , a transition from a Taylor-like dispersion regime to an "active" regime where the longitudinal dispersion coefficient increases such as :  $\frac{D_{||}}{D_0} \propto Pe^{2+\kappa}$ . The "active" regime is characterised by a relaxation time scale  $\tau_c/\tau_{taylor}$  that increases with the average flow velocity like  $U^\kappa$  with  $1.5 < \kappa < 2.1$ . The increase of relaxation time comes from the particles that get aligned in the flow direction reducing in turn the diffusivity in the gap. The beginning of the "active" regime is characterised by a depletion of the central part of the channel. Particles then accumulate in two regions close to the surfaces where the shear is high. The existence of high shear trapping of the bacteria and depletion at the centre of the channel at high  $Pe_f$  is in tandem with the experimental results of Rusconi et al. [11] and the numerical study of Vennamneni et al. [14]. Like in Vennamneni et al. [14], we also observed, for bacteria with small aspect ratio, that the high shear trapping regime is followed by a low shear trapping *i.e.* particles are trapped more at the vicinity of the centre with increase in shear rate and still the depletion at the centre deepens. Vennamneni et al. [14] also predicts a centerline collapse of the particle distribution for  $q > 2$ .

This final regime is not observed in our study, most likely because it requires a flow Péclet number well above 300 which is the largest value considered here. For the first time, the existence of both high shear and low shear trapping at large  $Pe_f$  for  $q = 0.5$  was observed. In this case, the accumulation was either at the centre of the channel, where the shear was zero or on the surface, where the shear was maximum. This indicated that, these particles, due to their unique swimming mechanism, tend to make big "jumps" from the highest to lowest shear regions across the flow lines in the channel gap.

The anomalous exponent  $\kappa$  was found to be very close to 2 for particle with aspect ratio less than 2. This value is consistent with the value obtained by a physical model for spherical particles. For larger  $q$ , the exponent  $\kappa$  decreases. A recent preprint [32] reports an asymptotic value of  $\kappa = 4/3 \simeq 1.33$  for  $q \rightarrow \infty$ ; this value obtained using multi-scale analysis is close to the value of  $\kappa \simeq 1.5$  obtained for the largest aspect ratio ( $q = 10$ ) considered in our study. Finally, we observe that reducing the aperture delays the transition to the "active" regime.

Additional diffusion term puts an end to the  $Pe^{(2+\kappa)}$  behaviour. A new regime is reached when the apparent diffusion coefficient in the gap becomes similar to the extra diffusion term. The distributions of the particles in the gap flatten again (like observed at small  $Pe$ ) and the longitudinal dispersion coefficient then scales again like Péclet to the square but with a new Péclet number based on the diffusion coefficient,  $D_m$ , instead of the diffusion coefficient  $D_0$ . We then have:  $\frac{D_{||}}{D_m} = 1 + \alpha Pe_c^2$  or equivalently  $\frac{D_{||}}{D_m} = 1 + \alpha (\frac{D_0}{D_m} Pe)^2$ .

## V. PERSPECTIVES

This study is the first step to a more complete description of dispersion of swimming bacteria that would include the heterogeneous and disordered structure of the flow observed in porous media. In the present study, we assume that the suspension is diluted in the bulk and that the particles are small in size such as there is no particle-particle interaction and the effect of particles on the flow field of surrounding fluid is negligible. However, we know that when the number of bacteria increases new phenomena like collective motion emerges [33] with effect on the effective viscosity [34, 35]. As a first step, this effect can be included in our model by introducing a local viscosity as function of the local shear and of the local bacteria concentration. This could be the



first step towards a comprehension of the effect of bacterial number on the macroscopic dispersion that would include hydrodynamic interactions between swimmers.

## ACKNOWLEDGMENTS

This work is supported by public grants overseen and by the French National Research Agency (ANR) through the "Laboratoire d'Excellence Physics Atom Light Mater" (LabEx PALM) as part of the "Investissements d'Avenir" program (ANR-10-LABX-0039) and by the ANR grant "BacFlow" ANR-15-CE30-0013. M.D. acknowledges the support of the Spanish Research Agency (10.13039/501100011033) and the Spanish Ministry of Science and Innovation through the project HydroPore(PID2019-106887GB-C31). H.A. acknowledged the support of CNRS 80IPRIME through the projet RootBac.

## Appendix A: Langevin equation for particle orientation

In this appendix, we show that the Langevin equation (2) preserves the magnitude of  $\mathbf{p}$  equal unity. Furthermore, we show the equivalence of the Langevin model to the two-dimensional model employed in the study by Rusconi *et al.* [11] by writing (2) in polar coordinates. First, we demonstrate that the magnitude is conserved. To this end, we write the Langevin equation for  $p^2(t) = \mathbf{p}(t) \cdot \mathbf{p}(t)$ . Using the Ito rule, we obtain

$$\begin{aligned} \frac{dp^2}{dt} &= 2\mathbf{p} \cdot (\mathbb{I} - \mathbf{p} \otimes \mathbf{p}) \left( \frac{q^2 - 1}{q^2 + 1} \mathbf{E} - \mathbf{W} \right) \mathbf{p} - 4D_R p^2 \\ &\quad - \sqrt{2D_R} \mathbf{p} \cdot \mathbf{p} \wedge \boldsymbol{\xi}_p + 4D_R p^2. \end{aligned} \quad (\text{A1})$$

As  $\mathbf{p} \cdot \mathbf{p} \wedge \boldsymbol{\xi}_p = 0$ , we have

$$\frac{dp^2}{dt} = 2(\mathbf{p} - p^2 \mathbf{p}) \left( \frac{q^2 - 1}{q^2 + 1} \mathbf{E} - \mathbf{W} \right) \mathbf{p}. \quad (\text{A2})$$

For  $p^2(t=0) = 1$ , the solution of this equation is constant  $p^2(t) = 1$ . Thus, the magnitude is unity and conserved.

In order to see the equivalence to the model by Rusconi *et al.* [11], we first write Eq. (2) in two dimension,

$$\begin{aligned} \frac{d\mathbf{p}}{dt} &= (\mathbb{I} - \mathbf{p} \otimes \mathbf{p}) \left( \frac{q^2 - 1}{q^2 + 1} \mathbf{E} - \mathbf{W} \right) \mathbf{p} - D_R \mathbf{p} \\ &\quad - \sqrt{2D_R} \boldsymbol{\rho}^\top \cdot \boldsymbol{\xi}_p, \end{aligned} \quad (\text{A3})$$

where  $\boldsymbol{p} = (p_2, -p_1)^\top$ . We now set  $p_1 = \cos(\theta)$  and  $p_2 = \sin(\theta)$ . The Langevin equation for the angle can be written in general as

$$\frac{d\theta}{dt} = A(\theta) + \sqrt{2B(\theta)}\xi. \quad (\text{A4})$$

We determine the drift and diffusion coefficients  $A$  and  $B$  by comparison with the equation for  $p_1 = \cos(\theta)$ . We can write

$$\begin{aligned} \frac{dp_1}{dt} &= -\sin(\theta)\frac{d\theta}{dt} - B(\theta)\cos(\theta) = F(\theta) - D_R\cos(\theta) \\ &\quad - \sqrt{2D_R}\sin(\theta)\xi_1, \end{aligned} \quad (\text{A5})$$

where we defined

$$F(\theta) = \boldsymbol{e}_1 \cdot \left[ (\mathbb{I} - \boldsymbol{p} \otimes \boldsymbol{p}) \left( \frac{q^2 - 1}{q^2 + 1} \boldsymbol{E} - \boldsymbol{W} \right) \boldsymbol{p} \right]. \quad (\text{A6})$$

with  $\boldsymbol{e}_1$  the unit vector in 1-direction. We substitute (A4) into (A5) to obtain

$$\begin{aligned} &-\sin(\theta) \left[ A(\theta) + \sqrt{2B(\theta)}\xi \right] - B(\theta)\cos(\theta) = \\ &F(\theta) - D_R\cos(\theta) - \sqrt{2D_R}\sin(\theta)\xi_1, \end{aligned} \quad (\text{A7})$$

By comparison, we find that  $B(\theta) = D_R$  and

$$A(\theta) = -\frac{F(\theta)}{\sin(\theta)}. \quad (\text{A8})$$

Thus, the Langevin equation for the angle  $\theta$  is given by

$$\frac{d\theta}{dt} = -\frac{F(\theta)}{\sin(\theta)} + \sqrt{2D}\xi. \quad (\text{A9})$$

The strain rate tensor for two-dimensional Poiseuille flow is  $E_{11} = E_{22} = 0$  and

$$E_{21} = E_{12} = \boldsymbol{\sigma} = -u_0 y / a^2 \quad (\text{A10})$$

and local vorticity is  $W_{11} = W_{22} = 0$  and

$$W_{21} = -W_{12} = \boldsymbol{\sigma}. \quad (\text{A11})$$

Thus, we obtain for  $F$

$$F = C_{12}p_2 - p_1^2 p_2 (C_{12} + C_{21}), \quad (\text{A12})$$

where we defined  $\mathbf{C} = \frac{q^2-1}{q^2+1}\mathbf{E} - \mathbf{W}$ . And for  $A = -F/\sin(\theta) = -F/p_2$ , we obtain

$$A = -C_{12} + p_1^2(C_{12} + C_{21}) \quad (\text{A13})$$

Now we note that

$$C_{12} = \sigma \left( \frac{q^2-1}{q^2+1} + 1 \right), \quad C_{21} = \sigma \left( \frac{q^2-1}{q^2+1} - 1 \right) \quad (\text{A14})$$

and therefore

$$\begin{aligned} A &= -\sigma \left( \frac{q^2-1}{q^2+1} + 1 \right) + 2p_1^2 \sigma \frac{q^2-1}{q^2+1} \\ &= \frac{u_0 y}{a^2} \left[ 1 + \frac{1-q^2}{1+q^2} \cos(2\theta) \right] \end{aligned} \quad (\text{A15})$$

where we used that  $p_1 = \cos(\theta)$  and  $\sigma = u_0 y/a^2$ . Thus, we obtain for the angle  $\theta$  the Langevin equation

$$\frac{d\theta}{dt} = \frac{u_0 y}{a^2} \left[ 1 + \frac{1-q^2}{1+q^2} \cos(2\theta) \right] + \sqrt{2D_R} \xi, \quad (\text{A16})$$

which is equivalent to the Langevin equation considered by Rusconi *et al.* [11].

## Appendix B: Numerical implementation

$$x(t) = x(t-\tau) + \tau V_s p_x(t-\tau) + \sqrt{2D_m \tau} \xi_x \quad (\text{B1})$$

$$y(t) = y(t-\tau) + \tau V_s p_y(t-\tau) + \frac{\dot{\gamma}_m H \tau}{2} [1 - [\frac{z(t-\tau)}{H}]^2] + \sqrt{2D_m \tau} \xi_y \quad (\text{B2})$$

$$z(t) = z(t-\tau) + \tau V_s p_z(t-\tau) + \sqrt{2D_m \tau} \xi_z \quad (\text{B3})$$

$$\begin{aligned} p_x(t) &= p_x(t-\tau) - \frac{\dot{\gamma}_m z(t-\tau) \tau}{H} [B p_x(t-\tau) p_y(t-\tau) p_z(t-\tau)] \\ &\quad - 2D_R \tau p_x(t-\tau) - \sqrt{2D_R \tau} p_y(t-\tau) \xi_{pz} + \sqrt{2D_R \tau} p_z(t-\tau) \xi_{py} \end{aligned} \quad (\text{B4})$$

$$\begin{aligned} p_y(t) &= p_y(t-\tau) + \frac{\dot{\gamma}_m z(t-\tau) \tau}{2H} [p_z(t-\tau) [B[1 - 2p_y^2(t-\tau)] + 1]] \\ &\quad - 2D_R \tau p_y(t-\tau) - \sqrt{2D_R \tau} p_z(t-\tau) \xi_{px} + \sqrt{2D_R \tau} p_x(t-\tau) \xi_{pz} \end{aligned} \quad (\text{B5})$$

$$\begin{aligned} p_z(t) &= p_z(t-\tau) - \frac{\dot{\gamma}_m z(t-\tau) \tau}{2H} [p_y(t-\tau) [B[2p_z^2(t-\tau) - 1] + 1]] \\ &\quad - 2D_R \tau p_z(t-\tau) - \sqrt{2D_R \tau} p_x(t-\tau) \xi_{py} + \sqrt{2D_R \tau} p_y(t-\tau) \xi_{px} \end{aligned} \quad (\text{B6})$$

The above equations (B1 - B6) were coded in MATLAB. The channel height varies from  $z = -H$  to  $z = H$  and the width varies from  $x = -W$  to  $x = W$  and we have chosen  $W \gg H$ .

The particles are initially uniformly distributed between  $-W$  and  $W$  in  $x$ -direction,  $-H$  and  $H$  in  $z$ -direction and all are situated at  $y = 0$ . The initial orientation angles  $\theta$  and  $\phi$  were uniformly distributed between  $0$  to  $2\pi$  and the initial orientations were given by:

$$p_x(0) = \sin\theta\cos\phi ; p_y(0) = \sin\theta\sin\phi \text{ and } p_z(0) = \cos\theta$$

The boundary condition is implemented as follows: if the position of particle crosses the boundary it is restricted to stay at the boundary until it reorients itself and flows back into the channel i.e. if  $x(t) > W$  or  $x(t) < -W$  the particle is restricted to stay at  $x(t) = W$  or  $-W$  until it reorients and translates itself back into the channel. The same condition is used for  $z(t)$  as well.

The above equations are for determining the position and orientation for one particle at any instant time ( $t$ ) provided its position and orientation of previous time step ( $t - \tau$ ) is known. The same equations are solved simultaneously for  $10^5$  particles and it is carried out for long times (in order to obtain the steady state profile across the channel gap)

### Appendix C: Convergence test

The choice of an integration time step  $\tau$  is a key parameter for performing the simulations. We chose the value of  $\tau$  as function of period of rotation at a given  $\dot{\gamma}_m$  value. The period of rotation is defined as:

$$T = \frac{2\pi}{\dot{\gamma}_m} \left( q + \frac{1}{q} \right)$$

It can be seen that for any given value of  $\dot{\gamma}_m$ ,  $q = 1$  would have the lowest  $T$  value. Therefore the choice of  $\tau$  was with respect to  $T(q = 1)$ . In order to determine the best choice of  $\tau$ , we performed the simulations for different  $\tau$  values for a high  $Pe$  case ( $\dot{\gamma}_m = 50$ ) and checked for the convergence of  $D_{||}/D_0$  values.

In Fig. 15, the choice of  $\tau$  for  $q = 1$  and  $2$  were  $T/50$ ,  $T/100$ ,  $T/200$ ,  $T/350$  and  $T/500$ . We

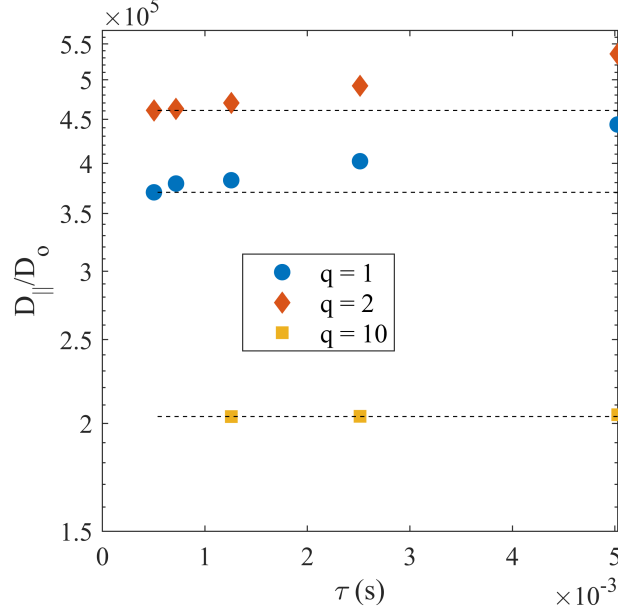


FIG. 15: Longitudinal dispersion coefficient  $D_{||}$  normalized by the diffusion coefficient in absence of flow  $D_0$  as function of the integration time  $\tau$  in s. The flow rate is such that  $\dot{\gamma}_m = 50s^{-1}$ . ( $\square$ )  $q=1$ , ( $\diamond$ )  $q=2$  and ( $\bullet$ )  $q=10$ . The dashed line represents the asymptotic value

observe the convergence of  $D_{||}/D_0$  to an asymptotic value as we decrease the value of  $\tau$ . We observe the convergence to happen from  $\tau = T/350$  onwards for  $q = 1$  and from  $\tau = T/200$  onwards for  $q = 2$ . For the case of  $q = 10$ , since the values converged at a higher  $\tau$ , we stopped the test for convergence at  $T/200$  itself. This convergence in the values of  $D_{||}/D_0$  is also corroborated with a convergence of steady state profiles of particles in the gap obtained for different integration time step  $\tau$  as shown by Fig. 16.

Based on the results of the convergence test carried out (c.f. Figs. 15 and 16), we chose  $\tau = T/350$  for  $q = 1$  simulations,  $\tau = T/200$  for  $q = 2$  simulations and  $\tau = T/50$  simulations.

#### Appendix D: Bacteria concentration profiles obtained for different flow Péclet

This appendix present the profiles obtained for different aspect ratio  $q$  for different flow Péclet.

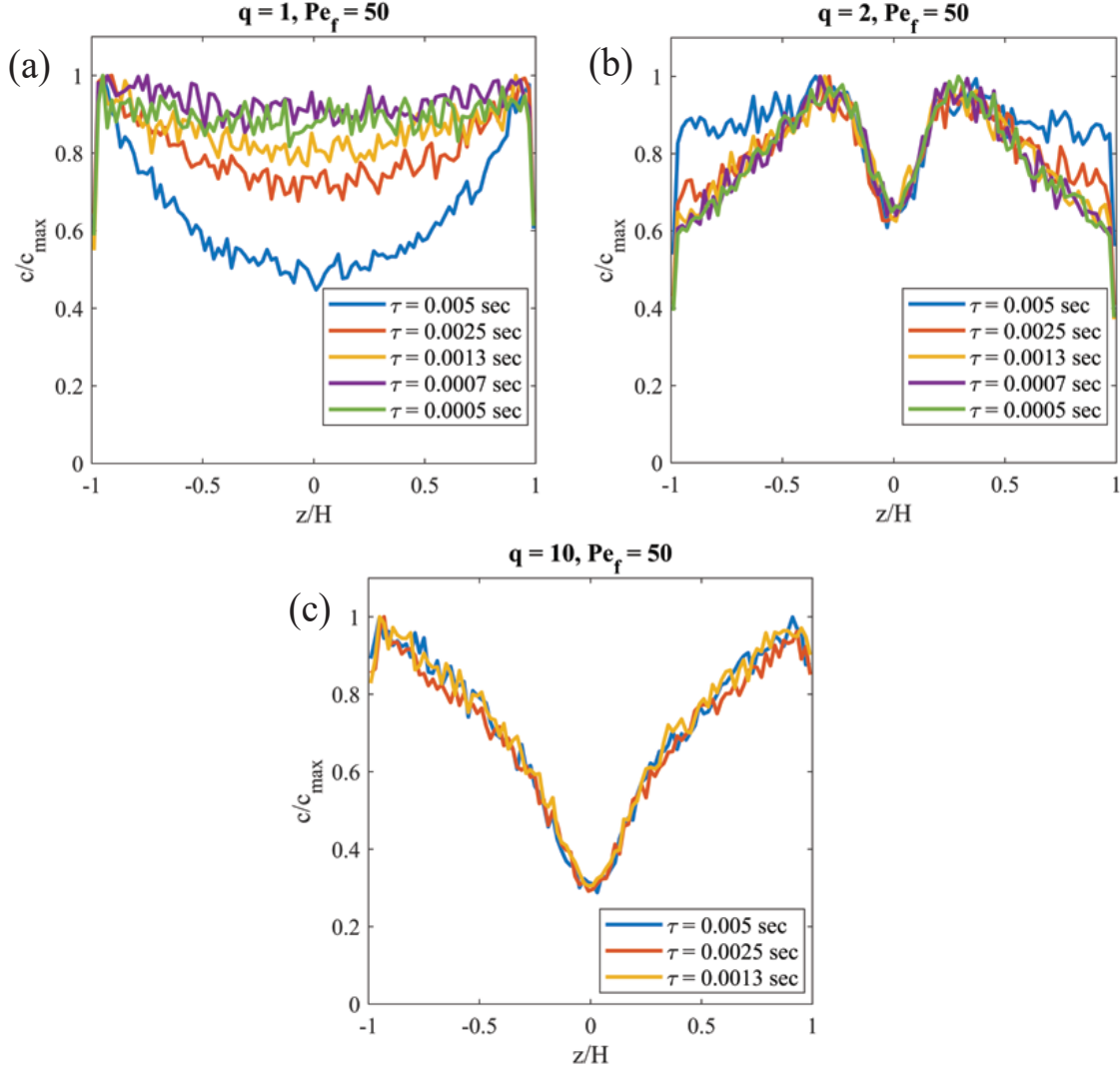


FIG. 16: Bacteria concentration profiles obtained for the same  $\dot{\gamma}_m = 50 \text{ s}^{-1}$  but for different integration time  $\tau$ . (a)  $q=1$ , (b)  $q=2$  and (c)  $q=10$ .

#### Appendix E: Proposition of a physical model for observed power law variation in $D_{\parallel}$

We propose the following model to estimate the value of  $\kappa$ . We know that  $D \sim \sigma_{U_p}^2 \tau_c$  and that  $\sigma_{U_p}^2$  scales with the average flow velocity like  $U^2$ . The pre-factor between  $\sigma_{U_p}^2$  and  $U_p^2$  depends on the asymptotic bacteria concentration profile in the gap. Our simulations validate this hypothesis. Thus, the additional component apart from the quadratic variation in the power law obtained, comes essentially from the relaxation time which increases with  $Pe$ .

At high  $Pe$ , the rotation period of the bacteria is set by the flow and scales like  $T \sim \dot{\gamma}_m^{-1}$  [12].

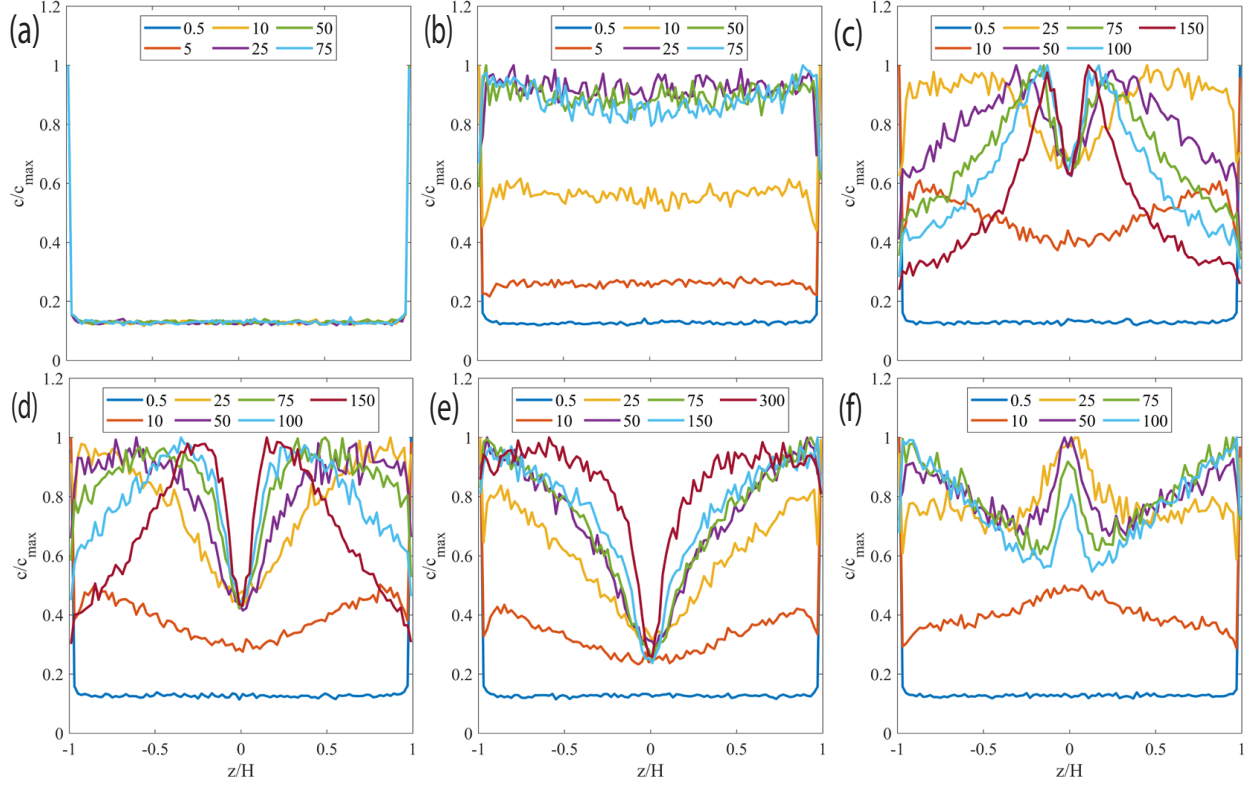


FIG. 17: Concentration profiles for decoupled case and different aspect ratios with SBC conditions as function of  $Pe_f$ . (a) Decoupled case, (b)  $q = 1$ , (c)  $q = 2$ , (d)  $q = 4$ , (e)  $q = 10$  and (f)  $q = 0.5$ . Data obtained for  $2H = 100\mu\text{m}$  and  $D_m = 0$ .

During one period of rotation, the amplitude of the motion of the bacteria in the gap is then  $l \sim V_s T$ . Since  $\dot{\gamma}_m = \frac{3U}{H}$ , we have  $l \sim H \frac{V_s}{U}$ . This means that, increasing the flow velocity reduces the amplitude of movement across the gap. The separation between time scales characterizing the particle orientation dynamics of characteristic time  $\tau_R = 1/D_R$  and those that characterize the period of rotation  $T$  along its helicoidal trajectory allows us to propose a model in which the particle diffuses by jumping between helicoidal trajectories. In this model, the diffusive time is  $\tau_R$ , and diffusion permits jumps of length  $l$ . The diffusion coefficient across the channel gap and the time to diffuse in the gap are then given by,  $D_z = \frac{2l^2}{\tau_R}$  and  $\tau_c = \frac{2H^2}{D_z}$ . We thus have,  $\tau_c = \frac{H^2 \tau_R}{l^2}$ . Since  $l \sim H \frac{V_s}{U}$ , the relaxation time is  $\tau_c \sim \tau_R (\frac{U}{V_s})^2$ .

From the above expression for the relaxation time  $\tau_c$ , we can deduce the dispersion coefficient in the direction of the flow using the relation  $D_{\parallel} \sim \sigma_{U_p}^2 \tau_c$ . Using the observation that  $\sigma_{U_p}^2 \sim U^2$ , we find  $D_{\parallel} \sim U^4$ . This model captures well the behavior of spherical particles ( $q = 1$ ), but over-

estimates the exponent  $\kappa$  measured for aspect ratios different from 1. The difference between the model and the simulation can be explained by the strong assumptions on which the model is based. We implicitly assumed that the jumps are independent without correlation with each other and that they follow a "not too wide" distribution. The observation of a preferential localization of particles across the channel gap at large flow velocities suggests that the jumps between trajectories probably retain some memory of previously occupied trajectories. The dependence of the relaxation time on the flow velocity is then probably more complex than predicted by our model.

- 
- [1] R. Rusconi, M. Garren, and R. Stocker, *Annual Review of Biophysics* **43**, 65 (2014).
  - [2] P. D. Frymier, R. M. Ford, H. C. Berg, and P. T. Cummings, *Proceedings of the National Academy of Sciences* **92**, 6195 (1995), publisher: National Academy of Sciences Section: Research Article.
  - [3] J. Hill, O. Kalkanci, J. McMurry, and H. Koser, *Physical Review Letters* **98**, 068101 (2007).
  - [4] G. Li, J. Bensson, L. Nisimova, D. Munger, P. Mahautmr, J. X. Tang, M. R. Maxey, and Y. V. Brun, *Physical Review E* **84**, 041932 (2011).
  - [5] T. Kaya and H. Koser, *Biophysical Journal* **102**, 1514 (2012).
  - [6] Marcos, H. C. Fu, T. R. Powers, and R. Stocker, *Proceedings of the National Academy of Sciences* **109**, 4780 (2012).
  - [7] G. Junot, T. Darnige, A. Lindner, V. A. Martinez, J. Arlt, A. Dawson, W. C. Poon, H. Auradou, and E. Clément, *Physical Review Letters* **128**, 248101 (2022), publisher: American Physical Society.
  - [8] A. J. T. M. Mathijssen, N. Figueroa-Morales, G. Junot, Clément, A. Lindner, and A. Zöttl, *Nature Communications* **10**, 1 (2019).
  - [9] R. Rusconi and R. Stocker, *Current Opinion in Microbiology* **25**, 1 (2015).
  - [10] G. Junot, N. Figueroa-Morales, T. Darnige, A. Lindner, R. Soto, H. Auradou, and E. Clément, *EPL (Europhysics Letters)* **126**, 44003 (2019), publisher: IOP Publishing.
  - [11] R. Rusconi, J. S. Guasto, and R. Stocker, *Nature Physics* **10**, 212 (2014).
  - [12] G. B. Jeffery, *Proceedings of the Royal Society of London. Series A, Containing Papers of a Mathematical and Physical Character* **102**, 161 (1922), publisher: Royal Society.
  - [13] B. Ezhilan and D. Saintillan, *Journal of Fluid Mechanics* **777**, 482 (2015), publisher: Cambridge University Press.



- [14] L. Vennamneni, S. Nambiar, and G. Subramanian, *Journal of Fluid Mechanics* **890**, A15 (2020).
- [15] L. Vennamneni, P. Garg, and G. Subramanian, *Journal of Fluid Mechanics* **904** (2020), 10.1017/jfm.2020.664, publisher: Cambridge University Press.
- [16] H. C. Berg, *E. coli in motion*, Biological and medical physics series (Springer, New York, 2004).
- [17] M. E. Cates and J. Tailleur, *EPL (Europhysics Letters)* **101**, 20010 (2013), arXiv: 1206.1805.
- [18] G. Junot, E. Clément, H. Auradou, and R. García-García, *Physical Review E* **103**, 032608 (2021), publisher: American Physical Society.
- [19] A. Dehkharghani, N. Waisbord, J. Dunkel, and J. S. Guasto, *Proceedings of the National Academy of Sciences* **116**, 11119 (2019).
- [20] M. Raible and A. Engel, *Applied Organometallic Chemistry* **18**, 536 (2004), \_eprint: <https://onlinelibrary.wiley.com/doi/pdf/10.1002/aoc.757>.
- [21] G. I. Taylor, *Proceedings of the Royal Society of London. Series A. Mathematical and Physical Sciences* **219**, 186 (1953), publisher: Royal Society.
- [22] R. Aris and G. I. Taylor, *Proceedings of the Royal Society of London. Series A. Mathematical and Physical Sciences* **235**, 67 (1956), publisher: Royal Society.
- [23] E. Clement, A. Lindner, C. Douarche, and H. Auradou, *The European Physical Journal Special Topics* **225**, 2389 (2016).
- [24] D. Saintillan, *Experimental Mechanics* **50**, 1275 (2010).
- [25] G. Jing, A. Zöttl, Clément, and A. Lindner, arXiv:2003.04012 [cond-mat, physics:physics] (2020), arXiv: 2003.04012.
- [26] A. Zöttl and H. Stark, *Physical Review Letters* **108**, 218104 (2012).
- [27] J. Elgeti and G. Gompper, *The European Physical Journal Special Topics* **225**, 2333 (2016).
- [28] M. Molaei, M. Barry, R. Stocker, and J. Sheng, *Physical Review Letters* **113**, 068103 (2014).
- [29] J. Saragosti, P. Silberzan, and A. Buguin, *PLOS ONE* **7**, e35412 (2012), publisher: Public Library of Science.
- [30] I. Frankel and H. Brenner, *Journal of Fluid Mechanics* **204**, 97 (1989), publisher: Cambridge University Press.
- [31] M. Dentz, J. J. Hidalgo, and D. Lester, *Transport in Porous Media* , 1 (2022).
- [32] L. Vennamneni, P. Garg, and G. Subramanian, arXiv preprint arXiv:2212.01817 (2022).
- [33] J. Gachelin, A. Rousselet, A. Lindner, and E. Clement, *New Journal of Physics* **16**, 025003 (2014), wOS:000332614300001.

- [34] V. A. Martinez, E. Clément, J. Arlt, C. Douarche, A. Dawson, J. Schwarz-Linek, A. K. Creppy, V. Škultéty, A. N. Morozov, H. Auradou, and W. C. K. Poon, Proceedings of the National Academy of Sciences **117**, 2326 (2020), publisher: National Academy of Sciences Section: Physical Sciences.
- [35] H. M. López, J. Gachelin, C. Douarche, H. Auradou, and E. Clément, Physical Review Letters **115**, 028301 (2015), publisher: American Physical Society.